

# Functional Liver Partition of DCE-MRI

*Zhiyi Wu*

# Functional Liver Partition of DCE-MRI

By

*Zhiyi Wu*

in partial fulfilment of the requirements for the degree of

**Master of Engineering**  
in Biomedical Engineering

at the Delft University of Technology,  
to be defended publicly on Thursday August 3, 2017 at 10:00 AM.

Supervisor: dr. F. M. Vos  
Thesis committee: dr. F. M. Vos, TU Delft  
Prof. dr. P. J. French, TU Delft  
MSc. T Zhang, TU Delft

# Acknowledgements

I would like to express my sincere gratitude to my supervisors, Prof. Frans Vos and Ph.D. Tian Zhang, for their guidance on my thesis project. They have given me many wise suggestions and motivated me. Tian has shared his valuable experiences in developing image segmentation and registration algorithms and gave a great favour to me at the beginning of this project. Prof. Frans has inspired me to think out of the box and analyse problems from multiple aspects. I am also grateful to receive help from all Imaging Physics members. They have helped me to know about the Netherlands better. Thanks to everyone who has supported me during this thesis project.

# Content

|  |    |
|--|----|
| Acknowledgements .....   | II |
| 1 Introduction .....   | 1  |
| 1.1 Motivation .....   | 1  |
| 1.2 Thesis Objectives .....  | 3  |
| 1.3 Outlines .....   | 4  |
| 2 Background Theory and Related Work .....   | 5  |
| 2.1 Overview .....   | 5  |
| 2.2 Anatomy of the functional liver partition .....  | 6  |
| 2.3 Image registration .....   | 7  |
| 2.3.1 Image registration basics .....  | 7  |
| 2.3.2 Modality-independent neighborhood descriptor (MIND) .....                                  | 9  |
| 2.4 Image segmentation .....   | 11 |
| 2.4.1 Image segmentation basics .....  | 11 |
| 2.4.2 New hybrid level set method .....  | 13 |
| 2.5 Vessel segmentation and functional liver partition .....                                     | 14 |
| 3 DCE-MRI Data Preprocessing .....   | 16 |
| 3.1 Overview .....   | 16 |
| 3.2 MRI protocol .....   | 17 |
| 3.3 DCE-MRI denoising using discrete wavelet transform .....                                     | 17 |
| 3.3.1 Discrete wavelet transformation basics .....   | 17 |
| 3.3.2 The application of discrete wavelet transformation in time-intensity data processing ..... | 19 |
| 3.4 DCE-MRI denoising using model fitting .....  | 20 |
| 3.4.1 Dual-inlet tow compartment liver perfusion model .....                                     | 20 |
| 3.4.2 Measurement of tissue concentration from DCE-MRI .....                                     | 22 |
| 3.4.3 Global arterial input function (AIF) and venous input function (VIF) measurement .....     | 23 |
| 3.4.4 TICs obtained from Sourbron's model .....  | 25 |
| 3.5 Comparison between DWT and model fitting methods .....                                       | 26 |
| 4 Vessel Segmentation Using Time-intensity Information .....                                     | 28 |
| 4.1 Overview .....   | 28 |
| 4.2 Spearman rank correlation .....  | 29 |
| 4.3 Mixing estimation map .....  | 31 |
| 4.4 Vessel segmentation using new hybrid level set method .....                                  | 33 |
| 4.5 Vessel segmentation method verification and comparison .....                                 | 35 |
| 5 Functional Liver Partition .....   | 38 |

|  |    |
|--|----|
| 5.1 Overview .....                                     | 38 |
| 5.2 Resection plane interpolation .....                | 39 |
| 5.3 Functional liver partition .....                   | 41 |
| 6 Discussion and Conclusion.....                       | 44 |
| 6.1 Overview .....                                     | 44 |
| 6.2 Limitations of hepatic vessel segmentation.....    | 45 |
| 6.3 Limitations of functional liver segmentation ..... | 46 |
| 6.4 Future Improvements .....                          | 47 |
| 6.5 Conclusions .....                                  | 48 |
| References .....                                       | I  |

# List of Figures

|   |    |
|---|----|
| Fig.1. The functional anatomy of the liver.....   | 6  |
| Fig.2. The schematic of the liver anatomy. The white strip in figure a is the falciform ligament. The green region in both figures a and b is the gallbladder fossa. The Cantlie's line crosses the middle hepatic vein used for left and right liver partition.....                    | 7  |
| Fig.3. Local self-similarity: A=a, B=b, C=c, D=d, E=e, F=f.....   | 10 |
| Fig.4. Deformable model curve representation using a distance transform: the evolvment of the 1D closed curve (a) in the image can be implicitly described by the 2D distance functions of (b). .....   | 12 |
| Fig.5. Level-set conventions. ....  | 13 |
| Fig.6. The schematic of vessel sub-branches used in the distance clustering method. ....  | 15 |
| Fig.7. The workflow of level-3 DWT process. ....  | 19 |
| Fig.8. The time-intensity profiles of a pixel in the liver. ....  | 20 |
| Fig.9. The schematic of the CA uptake process in liver.....   | 21 |
| Fig.10. The diagram of Sourbron's liver perfusion model. AIF: arterial input function, VIF: venous input function, $T_A$ and $T_V$ : time delay of AIF and VIF, $F_A$ and $F_V$ : arterial and venous plasma flow, $V_E$ : extracellular volume, $K_i$ : intracellular uptake rate..... | 22 |
| Fig.11. The schematic of AIF model.....   | 24 |
| Fig.12. AIF and VIF obtained from modified Orton's model.....   | 25 |
| Fig.13. Time-intensity curves obtained from Sourbron's liver perfusion model.   | 26 |
| Fig.14. TICs after DWT filtering. The red and blue curves are TICs of a hepatic vein voxel and a liver voxel. ....  | 27 |
| Fig.15. The division of the whole enhancement period. (IVC: inferior vena cava) .....   | 30 |
| Fig.16. The correlation coefficient maps with portal vein, hepatic vein and liver TICs.....   | 31 |
| Fig.17. The schematic of the linear mix assumption. The y axes are the tissue intensity while the x axes are the time. ....   | 32 |

Fig.18. The mixing estimation maps. The maps (a), (b), (c), and (d) represent the fraction of the corresponding vessels in the linear combination. In IVC (inferior vena cava) fraction map (c), the boundary has high fractions. The liver mask was dilated twice to ensure that all vessel voxels are included. Therefore, those boundary voxels which are removed before the vessel segmentation, are not from liver leading to high values in IVC map. ....33

Fig.19. The figures of mixing estimation maps, correlation maps and summation maps of the selected slices. (IVC: inferior vena cava).....34

Fig.20. The obtained 3D vessel structure. (IVC: inferior vena cava) .....34

Fig.21. The mean TIC of each vessel mask. (IVC: inferior vena cava).....35

Fig.22. The comparison between the manual and proposed segmentations. Figures A and B are results of the proposed segmentation while figures C and D are results of the manual segmentation. ....36

Fig.23. Determination of three landmarks on hepatic veins and one on IVC. The left figure shows the X-Y plane projection of the vessel mask. The red points in the right figure indicate the selected landmarks for resection planes construction. ....39

Fig.24. Determination of three landmarks for the first segment. The left figure shows the X-Y plane projection of the vessel mask. The red points in the right figure indicate the selected landmarks for resection plane construction. Point 3 on the portal vein bifurcation edge while the other two 1 and 2 points on the IVC edge were selected. ....40

Fig.25. Determination of horizontal resection planes. The projection image consists of the right, middle and left portal vein, the corresponding yellow, pink and blue regions. The two red lines slice 1 and slice 2 indicate the slice locations of the right and left portal vein bifurcations respectively. ....40

Fig.26. Workflow of the proposed functional liver partition. ....42

Fig.27. Liver functional segments. ....42

Fig.28. Image (a) is the minus product of the last DCE image frame and the first DCE image frame. Image (b) is the portal vein correlation map. ....45

Fig.29. Bifurcation of left hepatic vein. (IVC: inferior vena cava) .....47

# Introduction

## 1.1 Motivation

Magnetic resonance imaging (MRI) is a versatile and radiation free radiological imaging modality that has been proven to be a useful tool in the diagnosis and evaluation of a variety of disorders. Compared with other imaging modalities such as CT and PET, MRI is more sensitive to subtle changes within soft tissues. Because the contrast depicted in MRI is typically generated by the density and the relaxation times ( $T_1$  and  $T_2$ ) variations of tissue hydrogen nuclei [1].

There are several different types of MR techniques and one is the dynamic contrast-enhanced (DCE) MRI which has been proposed to be an effective tool in analyzing the function of organs such as the liver, kidney and breast [1]. The contrast agent (CA) is injected intravenously into the patient and a series acquisitions of MR images are required before and after the injection, thereby recording MR signal intensity of each image voxel over time. The CA enters a tissue through the blood supply network and accumulates in the tissue until the local CA concentration reaches equilibrium [9]. The CA-induced MR signal intensity variation enables the quantification of physiological parameters related to blood flow, vessel permeability and tissue volume fractions using appropriate mathematical models [1].

In liver surgeries, resection of lesions could inevitably reduce the liver volume hence sacrificing the healthy liver cells. Therefore, in surgical planning, the volume of

the remnant region as well as the pathological region are required to be estimated precisely. Couinaud [17] proposed that the liver can be divided into eight segments as each of them has an independent circulatory system. Manual segmentation of each segment as well as the vessels are tedious and time-consuming tasks. Therefore, an increasing number of automatic or semi-automatic segmentation methods are proposed especially for CT images due to the high image resolution and the absence of intensity inhomogeneities [2], [3], [4], [8]. The two mature and widely used segmentation methods are: histogram based thresholding segmentation and vessel enhancement filtering.

Since the signal intensities in the liver parenchyma, vessels and nodules are relatively homogeneous, the histogram of the total liver region can be interpreted as a mixed model of three Gaussians functions. From the trimodal histogram, two thresholds can be estimated to segment each type of tissues. Although the thresholding method is straightforward and easy to implement, it is not robust since the tissue intensities vary markedly for different patients. Especially in MRI, intensity inhomogeneities often lead to overlap between the adjacent Gaussian distributions of different tissues. As a result, the thresholds are difficult to be determined due to the unobvious trimodal profile. Besides, prevalent MR signal inhomogeneities are also a reason that most region-based methods could not give an accurate segmentation [35].

Then a bias field has been introduced to the image model to deal with the presence of intensity inhomogeneities [42], [46], [47]. The model assumes that the image intensity consists of a bias field, the true image and the Gaussian noise. The bias field mimics the source of the intensity inhomogeneities while the true image represents the intrinsic physical property of the tissues. Considering the tissue specified true image and the locally constant bias field, a global clustering criterion can be defined and converted into level set energy function for segmentation.

Meanwhile, the vessel enhancement filtering proposed by Frangi [6] and diffusion enhancing method based on Frangi proposed by Manniesing [7] have been proved to be an effective processing technique in vessel segmentation [5], [8], [10]. The vesselness structure is first detected by analyzing the Hessian matrix of the image. The anisotropic diffusion in the vessels leads to an ellipsoid eigenvalues distribution which makes the vessel different from other structures. With the obtained eigenvalues and vesselness function, the diffusion tensor is defined to preserve the vessels. After

filtering the image based on this tensor, the vessels are enhanced allowing the region grow method to segment the vessels from the image [10].

All these aforementioned methods intend to achieve the segmentation using high contrast 3D images. But in the DCE-MRI, both the vessel and liver are enhanced simultaneously, thus leading to the insufficient intensity contrast. One of the most widely used segmentation methods in DCE-MRI is time-intensity curve (TIC) shape analysis [54], [55] which differentiates voxels by quantifying TIC characteristics. This method fulfills the voxel characterization in a direct and easy way, however requiring many thresholds.

Besides, the hepatic tumors are also the challenge for vessel segmentation, because they contain abundant vessels. Thus, this thesis suggested an automatic and robust vessel segmentation method based on 4D DCE-MR images, which is used for further functional liver partition.

## 1.2 Thesis Objectives

This project is dedicated to segmentations of both hepatic vessels and functional liver segments and their application to liver surgery planning. The development of clinically applicable hepatic vessels delineation and liver segments partition algorithms for DCE-MRI is the major objective of the thesis. Besides, the preprocessing of DCE-MR images is computed using two different methods.

The thesis project mainly contains the following steps:

1. The preprocessing of DCE-MR images for noise filtering.
2. The segmentation of the hepatic vessels (portal vein, hepatic veins and inferior vena cava) from 4D abdominal DCE-MR images.
3. The definition and interpolation of the resection planes using the location of corresponding blood vessels.
4. The partition of the functional liver segments.

## 1.3 Outlines

In the first chapter, the objective of this project and some available hepatic vessel segmentation methods are introduced. The second chapter illustrates the background information on liver anatomy and the related image segmentation and registration methods of this project. In Chapter 3, two preprocessing methods for DCE-MRI are introduced and the comparison between them is given at the end of this chapter. The image processing algorithms developed in this thesis are introduced in the following two chapters. Chapter 4 shows the hepatic vessel segmentation algorithm while Chapter 5 illustrates the functional liver partition algorithm. In the last chapter, the limitations and possible improvements of all aforementioned algorithms are discussed and the conclusions are also given at the end of this chapter.

## Background Theory and Related Work

### 2.1 Overview

In Section 2.2, the anatomical background of the functional liver partition is introduced. Subsequently, in Section 2.3, general principles of image registration and a review of the modality independent-neighborhood descriptor (MIND) deformable registration method are demonstrated. Finally, in Section 2.4, image segmentation basics and a review of the hybrid level-set method are reviewed.

## 2.2 Anatomy of the functional liver partition

Liver anatomy considers the morphological and functional aspects of the liver [18]. The morphological anatomy divides the liver into four lobes based on external appearance: right, left, quadrate and caudate [18]. The functional liver anatomy takes into account the internal features of hepatic vessels and biliary ducts branching. On the basis of the liver functional anatomy, the French surgeon Claude Couinaud firstly proposed that the liver can be divided into eight functionally independent segments, as shown in Fig.1 [17]. Each segment of the liver is supplied by a unique circulatory system consisting of two vascular inflows, an outflow and a biliary drainage. The distribution of the vessels dominates the partitioning in segments .

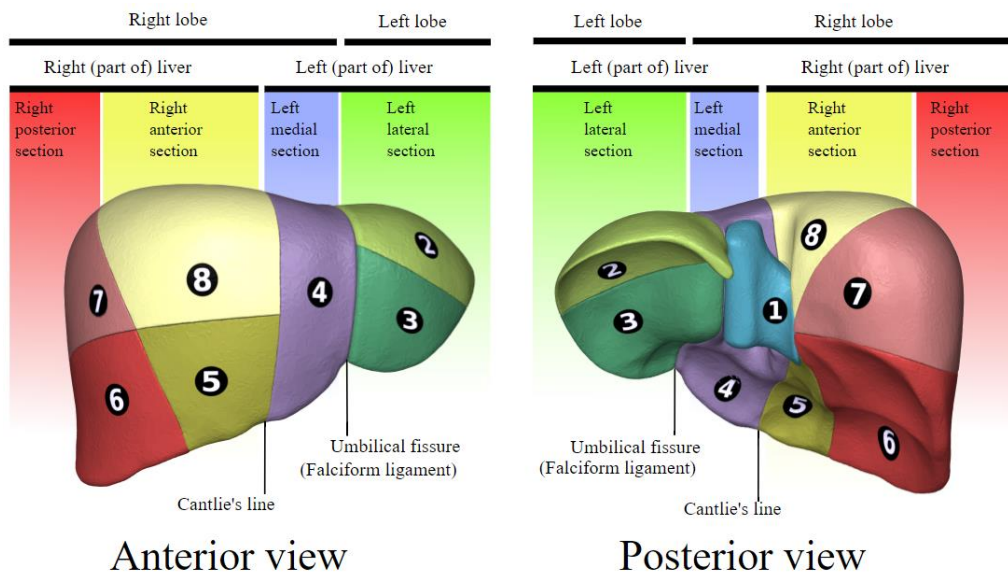


Fig.1. The functional anatomy of the liver [53].

Clinically, radiologists manually segment the liver on cross-sectional images by extrapolating three lines [17] [18]. The first line along the falciform ligament (see Fig.2) superiorly to the inferior vena cava (IVC) divides the left lobe. The second line from the gallbladder fossa (see Fig.2) superiorly along the middle hepatic vein to IVC segments the liver into right and left lobes. The third line along the right hepatic vein from IVC to the lateral liver margin separates the right lobe. Due to the large image volumes and limited image resolution, the manual partition of the whole liver is a time-consuming and subjective task. Therefore, an automatic method is in demand for more

accurate and fast partition.

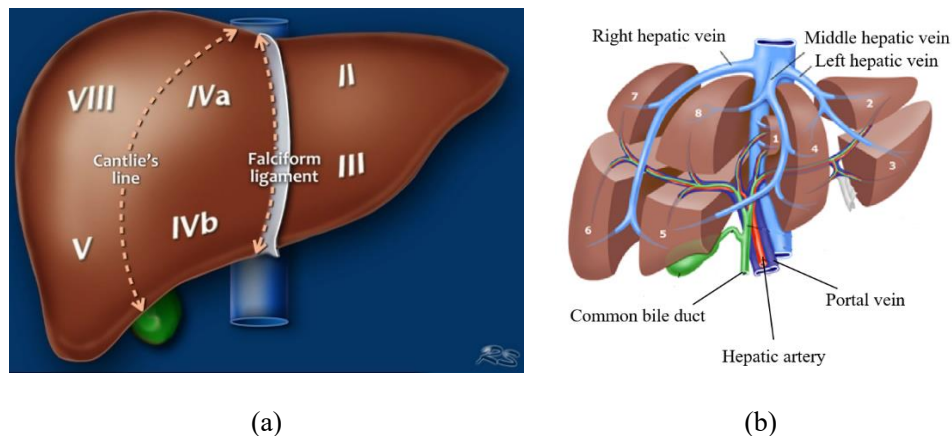


Fig.2. The schematic of the liver anatomy. The white strip in figure a is the falciform ligament. The green region in both figures a and b is the gallbladder fossa. The Cantlie's line crosses the middle hepatic vein used for left and right liver partition [17].

Functional liver partition is also an effective tool for surgery planning [18]. It intends to help surgeons to gain a comprehensive understanding of the potential risks, thereby making more reliable plans. In the resections which aim to remove a lesion or split the liver for the transplantation, the liver volume and related functions will be inevitably sacrificed. The remnant liver volume estimation is vital for those patients who have a low liver regeneration power. Besides, the resection itself also could lead to regional dysfunctions if the vessels are truncated during the surgery. As a result, all these risks require precise prediction.

## 2.3 Image registration

### 2.3.1 Image registration basics

Medical images have been widely used for the diagnosis, treatment planning and guidance and diseases progression monitoring in the healthcare field. Due to the breathing and motion of the patient during the scan, organs can appear deformed in the images [19]. In order to solve this problem, image registration has been proposed to align different images by accurately relating the corresponding information between them.

Registration is defined as the spatial transformation between a reference image and a target image [19], [20]. Most registration methods contains the following four components according to Brown [20]:

1. Feature space.
2. Transformation model.
3. Similarity metric.
4. Search strategy.

The implementation of each component requires a comprehensive consideration. The feature space contains image information that is used to define the similarity metric. The search for the optimal transformation in the transformation model is determined by the search strategy. The whole registration process ends until the similarity measure of the selected transformation model stops decreasing.

According to the information used in the similarity metric definition, registration methods can be mainly divided into two classes: the intensity- and feature-based methods [20]. Intensity-based similarity measures intensity differences, intensity cross-correlation and information theory. The sum of squared differences (SSD) [21], [22], Pearson's correlation [23], [24] and mutual information (MI) [25], [26] are three of the most commonly used information theories. The assumption behind the intensity-based approaches is that the corresponding structures in different images should have correlated intensities. However, in DCE-MRI, the liver voxel intensities increase over the scan due to the injected contrast agent. Additionally, the breathing and motion of patients could induce the intensity variations. Therefore, most intensity-based methods did not yield an accurate registration for DCE-MRI.

In feature-based methods, the registration is performed by finding the correspondence of a limited set of landmarks or segmented structures extracted from images [20], [27], [28]. Relating the corresponding features between two images, a transformation is determined to map a target image to a reference image. However, the identification of landmarks or organs of interest could be a difficult task and the inaccuracies in feature extraction have serious impacts on the registration. Besides, those features have to be invariant to possible image deformations, thereby demanding for the high robustness of the feature extraction algorithm. Therefore, instead of extracting the features directly, many image descriptors have been proposed to represent image features based on second-order statistics, parametric models and coefficients

obtained from an image transform [31]. Then the registration is conducted by finding the correspondences between image descriptors.

In the medical image processing field, image descriptors are mainly used to describe local features instead of global features. The global features such as image color and texture cannot differentiate foreground from background of an image. Image patches are applied to further define local features. The image descriptors are assumed to be invariant to image scaling, rotation, translation as well as noise within each patch [28], [29], [31]. In this study, the modality-independent neighborhood descriptor (MIND) [30] which characterizes each image voxel using the local self-similarity, is selected in this study.

### 2.3.2 Modality-independent neighborhood descriptor (MIND)

The MIND method is a deformable multimodal registration technique based on the concept of local self-similarity (see Fig.3) proposed by Buades [32]. The image descriptor enables the representation of the local image structure regardless of the intensity distribution across two images. Besides, the patch-based similarity measurement allows easy capture of image features such as edges, corners and textures which are often useful features in a correspondence measure.

MIND describes a local neighborhood as expressed below:

$$MIND(I, x, r) = \frac{1}{n} \exp\left(-\frac{D_p(I, x, x+r)}{V(I, x)}\right) r \in R \quad (1)$$

where  $I$  is an image,  $r$  is an offset within the size  $R \times R$  search region around position  $x$  and  $n$  is a normalization constant limiting the maximum to be 1. The distance measurement  $D_p$  between the voxels  $x_1$  and  $x_2$  is the sum of squared differences (SSD) of all voxels within the two patches  $P$  centered at  $x_1$  and  $x_2$ :

$$D_p(I, x_1, x_2) = \sum_{p \in P} (I(x_1 + p) - I(x_2 + p))^2 \quad (2)$$

and  $V(I, x)$  is the mean of the patch distances within the neighborhood  $N$ ,  $num(N)$  is the number of voxels inside  $N$ :

$$V(I, x) = \frac{1}{num(N)} \sum_{p \in P} D_p(I, x, x+n), n \in N \quad (3)$$

In order to reduce the computational complexity and the influence coming from non-rigid deformations, the six neighborhood search region is selected.

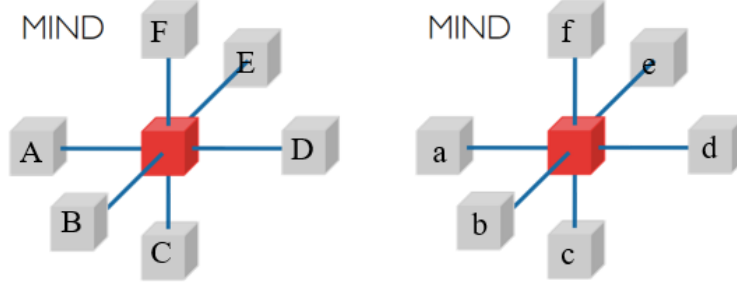


Fig.3. Local self-similarity: A=a, B=b, C=c, D=d, E=e, F=f.

Then the similarity metric of this registration method is obtained by the similarity term  $S(x)$  defined as:

$$S(x) = \frac{1}{|R|} \sum_{r \in R} |MIND(I, x, r) - MIND(J, x, r)| \quad (4)$$

in which  $I$  and  $J$  are two images.

The search strategy of MIND registration is to minimize the cost function with respect to the deformation field  $u = (u, v, w)^T$ , as shown in Eq.(5):

$$\arg \min_u \sum_x S(I_1(x), I_2(x+u))^2 + \alpha \text{tr}(\nabla u(x)^T \nabla u(x)) \quad (5)$$

In addition to the nonlinear similarity  $S$ , a diffusion regularization term is also included in this equation to ensure the smoothness of the deformation field. The balance between the similarity term and the regularization term is controlled by the parameter  $\alpha$ .

In all, MIND considers the whole image as the sum of many individual image patches and assumes a transformation must exist between two similar patches. This MIND method exceeds the prementioned intensity-based methods because the intensity uncertainties induced by artifacts as well as intensity inhomogeneities in DCE-MRI hinder the similarity measurement using intensity information.

## 2.4 Image segmentation

### 2.4.1 Image segmentation basics

Image segmentation is a critical step in image processing, facilitating the delineation, characterization and visualization of ROI in medical images. Implementing segmentation manually by radiologists is time-consuming and subjective. Therefore, many automatic segmentation approaches have been proposed to delineate and extract an anatomical structure fast and accurately. Three of the most common liver segmentation approaches were atlas-based, intensity-based and model-based [35].

The atlas-based methods involve the probabilistic atlas (PA) [36], [37] relying on a pre-constructed library of well-build shape models of the liver. The PA is built with massive training datasets and used as the standard liver. The segmentation of individual liver is performed by finding correspondences between the standard and individual livers. This approach is fully automatic and works well in normal liver. However, the available PV library is limited to a finite number of example shapes and not easy to be constructed. Besides, this shape fitting is only applicable to the healthy liver.

Common intensity-based approaches include region growing and gradient vector flow (GVF) [38]. The region growing method compares all the neighbor voxels around the initial seed points and then, includes the voxels having similar intensities to the seeds [39]. The object boundary is characterized by a drastic intensity change, thereby requiring high image contrast between the object and the background. Meanwhile, the GVF starts with a user defined curve [40]. The curve expands driven by intensities within the initial curved region and converges as the image gradient peaks. These semi-automatic methods require user's interaction for the algorithm initialization. They work well when object boundaries are sharp and clear. Unfortunately, the liver boundaries are usually obscure, which could force the contour to overshoot at such boundaries.

In model-based methods known as level set, curves or surfaces deform under the influence of internal and external forces to delineate the object [43], [44]. The internal forces coming from image intensities intend to preserve the smoothness of the model. The external forces originating from image gradients drive the model toward the target position.

The level set geometric model uses a distance transformation to bring the model

shape into a higher dimension, as shown in Fig.4: the 1D closed line (a) is transformed into the 2D surface (b) via the scalar distance function. The interface defines two regions, namely the region  $R_C$  above the red surface and the background  $R_B$  below. The model shape is represented implicitly as following [44]:

$$\Phi_C(x) = \begin{cases} 0, & x \in C \\ > 0, & x \in R_C \\ < 0, & x \in R_B \end{cases} \quad (6)$$

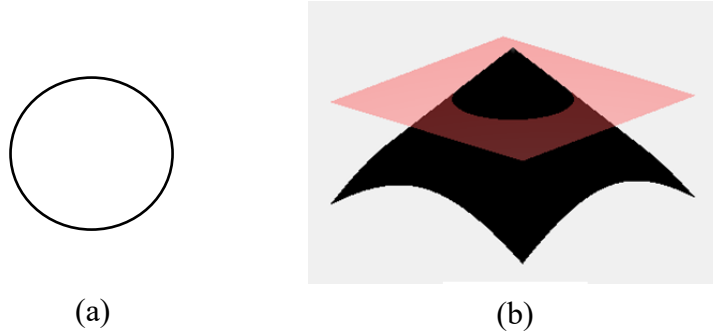


Fig.4. Deformable model curve representation using a distance transform: the evolvement of the 1D closed curve (a) in the image can be implicitly described by the 2D distance functions of (b).

Unlike the two dimensional region growing and active contour approaches, the three dimensional surface in level set could follow topology changes such as breaking and merging of the object [36],[35]. The contour evolution process witnesses the minimization of an energy cost function of the external and internal forces. The external force is inversely proportional to the image gradient. This inverse relation facilitates the model to attach to the strong edges or surfaces with local maximal image gradient. Therefore, this method can be applied to DCE-MR images due to their sufficient gradient between the object and the background. The internal force preserves the smoothness of the segmented liver boundaries. In GVF, the curve includes the surrounding voxels which have similar intensity to the curved region average intensity. However, due to the prevalent intensity inhomogeneities in MRI, this intensity-based similarity measure cannot yield an accurate segmentation. Contrarily, the single intensity threshold  $\mu$  (see Eq.(7)) used in level set reduces the dependence on voxel intensities and the threshold can be adjusted for different cases. In our study, a new hybrid level set method was applied for liver segmentation.

## 2.4.2 New hybrid level set method

The new hybrid level set method is one of the image segmentation methods in the level set framework. In the traditional edge-based level set methods, only boundary information is used to drive the front propagation of the contour and thus the contour might leakage at those weak edges. The proposed new hybrid level set method combines the boundary information with the region information to achieve object delineation and prevents boundary leakage simultaneously [45]. Fig.5 illustrates the level set conventions applied in this method [45]. A Heaviside function  $H(\phi)$  is defined with respect to the distance transform to define in and outside points of the segmentation.

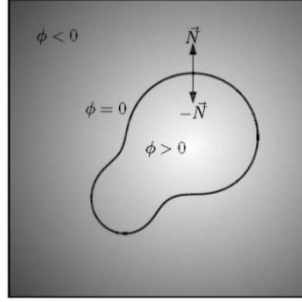


Fig.5. Level-set conventions. [45]

The cost function of this method is defined as the following equation:

$$\varepsilon(\phi) = -\alpha \int_{\Omega} (I - \mu) H(\phi) d\Omega + \beta \int_{\Omega} g |\nabla H(\phi)| d\Omega \quad (7)$$

where  $I$  is the image to be segmented,  $\mu$  is the intensity threshold,  $\Omega$  is the object domain,  $g = g(|\nabla I|)$  is the boundary feature function related to image gradient while  $\alpha$  and  $\beta$  are weights controlling the contour propagation and smoothness respectively. The first term in Eq.(7) is the region term which separates the image into object and background regions and also prevents leakage. The minimization of this single term forces the contour to reach the object surface. The second edge term encourages the contour to attach to the boundaries with maximum image gradient and adjust the smoothness of the contour. If the evolution starts with the initial contour being inside the object region, the region term dominates and drives the contour to expand. Once moving into the background region, the edge term becomes dominant and forces the contour to contract. As a result, a dynamical equilibrium is obtained at the object

boundary.

The minimization of the cost function above is performed by solving the corresponding partial differential equation (PDE) constructed as:

$$\phi_t = |\nabla \phi| \left[ \alpha(I - \mu) + \beta \operatorname{div} \left( g \frac{\nabla \phi}{|\nabla \phi|} \right) \right] \quad (8)$$

Subsequently, the scalar function  $\phi$  is iteratively updated using  $\bar{\phi}^k = \phi^k + \Delta_t \alpha(I - \mu)$  with a predefined time step  $\Delta_t$  and solving the PDE via the additive operator splitting (AOS) approach [45]. The whole process can be expressed as:

$$\phi^{k+1} = \phi^k \left( 1 - \Delta_t \sum_{l=1}^m A_l(\phi^k) \right)^{-1} + \alpha(I - \mu) \quad (9)$$

where  $A_l$  is the AOS operator.

## 2.5 Vessel segmentation and functional liver partition

Vessel segmentation intends to identify vessel voxels from the image using mainly three types of information: voxel intensities, diffusion characteristics and time-intensity information [2]. Due to the presence of intensity inhomogeneities in MRI, the intensity-based methods such as histogram-based thresholding [4], cannot give an accurate segmentation. Besides, the thresholds cannot be easily determined from the histogram owing to the intensity overlaps.

Anisotropic diffusion in vessels is widely used in the vessel segmentation to reduce noise [6], [7]. An ellipsoid eigenvalues distribution as generated to steer the anisotropic diffusion. Subsequently, vessels can be detected by analysing the Hessian matrix which measures the second order intensity derivations of each image voxel [5]. In such a vessel enhanced image, approaches such as region growing carry the segmentation.

TIC shape analysis is one of the most widely used approaches in DCE-MRI processing [55]. It quantifies time-intensity curve characteristics. Knowing the quantified characteristics such as time to peak, enhancement maximum and enhancement onset time, a decision tree can be constructed and used for segmentation.

TIC shape analysis intends to segment the vessels from 4D data. Nevertheless, its

segmentation requires many thresholds. The image data variations between different cases could reduce its reproducibility. This approach works well when the differences between TICs are significant. In our study, the partial volume effect occurring in small vessels and vessel boundaries leads to similar TICs. Accordingly, voxels are difficult to be differentiated using TIC shape analysis. Intensity-based and diffusion-based methods achieve the segmentation based on 3D high contrast images. As both the liver and vessels are enhanced in DCE-MRI simultaneously, the contrast between them is insufficient especially for the small vessels owing to the partial volume effect. This low image contrast could make the vessel eigenvalues distribution less distinguishable from other structures and thereby hinder the vessel detection especially at conjunction regions. As a result, the vessels might interrupt requiring the voxels interpolation. Except the insufficient contrast, the low resolution of each 3D image frame (128×128×44 voxels) in our study than CT images (512×512×180 voxels) in Luu's study [8] also requires an adapted vessel segmentation method.

After vessel segmentation, the functional liver partition intends to sort liver voxels into eight independent segments based on the locations of the vessels. Two of the available approaches are distance clustering and resection plane interpolation [61], [63]. In the distance clustering algorithm, the locations of the vessel sub-branches are used to sort the voxels by finding the nearest distance from the voxel to a certain sub-branch (see Fig.6). The limited image resolution in our study makes the full segmentation of vessel sub-branches to be a challenge. In the resection plane interpolation method, the resection planes are constructed based on vessels and interpolated into the liver for partition. Therefore, locations of the vessel main branches are required.

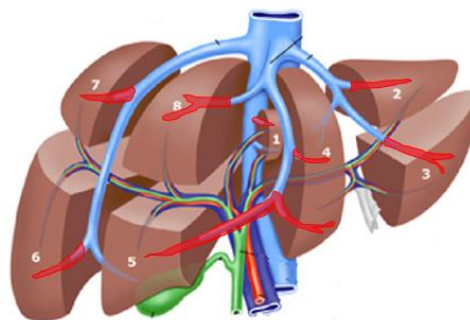


Fig.6. The schematic of vessel sub-branches used in the distance clustering method.

## DCE-MRI Data Preprocessing

### 3.1 Overview

In Section 3.2, the basic MR technical settings applied in our study are given. Subsequently, in Section 3.3, the discrete wavelet transform (DWT) is introduced for filtering the DCE-MRI. In Section 3.4, we demonstrate on how the DCE-MRI data are fitted to the liver perfusion model proposed by Sourbron to filter the noise and other required processing steps for model fitting are also introduced. Finally, in Section 3.5, the results obtained using both DWT and model fitting methods are analyzed and compared.

## 3.2 MRI protocol

Liver specific contrast agent (Gd-EOB-DTPA, Primovist™, Bayer pharmaceutical) is adopted in our study. It is a paramagnetic compound of which half of the dose is taken up by the normal functioning hepatocytes while the other half is excreted by the kidney. This contrast agent shortens the T1 relaxation times of protons resulting in higher signal intensity on T1-weighted images.

The DCE-MRI dynamic protocol (3D T1-weighted spoiled gradient echo) was performed on a 3T Philips scanner to acquire DCE-MRI data from 11 patients. MRI protocol parameters were as follows: TE/TR = 2.3/3.75ms, FA = 15°, FOV = 128×128×44, voxel size = 3×3×5mm<sup>3</sup>, acquisition time = 2.141s per volume; the sampling interval was 2.141s for volumes 1-81, 30s for volumes 82-98 and 60s for volumes 99-108. The total scan period was about 20 minutes. Patients held their breathing during the acquisition of volumes 13-22, 33-42, 61-70 and 79-108.

The registration and segmentation of DCE-MR images were performed using a method based on MIND proposed by Tian Zhang [48] and new hybrid level set approach [45] respectively. The liver segments partition method introduced below was performed within the obtained liver mask.

## 3.3 DCE-MRI denoising using discrete wavelet transform

### 3.3.1 Discrete wavelet transformation basics

The presence of noise in medical images could suppress and blur vital features and details. Various approaches have been proposed to denoise the images known as spatial filtering techniques, frequency domain filtering techniques and the discrete wavelet transform [49], [50], [51]. Conventional spatial filtering techniques remove the high-frequency noise through a convolution process which requires high computational cost. Frequency domain methods could balance the image denoise between the computational cost but they results in an overly smoothed images. Large signal intensity

gradients occurring in image edges or tissue boundaries could become smooth due to the trigonometric fitting in Fourier transform. Hence, the discrete wavelet transform approach capable of effectively removing noise without too much loss of image sharpness is proposed and selected in this study [49].

In discrete wavelet transform, the discrete input signal is represented by a series of shifted and scaled versions of the mother wavelet in the wavelet domain. After the transform, the signal is decomposed into two vectors of approximated and detailed coefficients respectively. With the approximated coefficients, a smooth and denoised signal can be reconstructed. The decomposition is defined as Eq.(10) where  $x(t)$  is the input signal,  $b$  is the shift factor,  $a$  is the scale factor and  $\Psi$  is the mother wavelet [50].

$$X(b, a) = \frac{1}{\sqrt{a_0^m}} \int_{-\infty}^{\infty} x(t) \Psi\left(\frac{t-nb}{a_0^m}\right) dt \quad (10)$$

In this project, Daubechies 4 mother wavelet was selected as its iterations overlap accurately pick up the small signal variations [51]. It provides four scaling function coefficients  $(h_0 = \frac{1+\sqrt{3}}{4\sqrt{2}}, h_1 = \frac{3+\sqrt{3}}{4\sqrt{2}}, h_2 = \frac{3-\sqrt{3}}{4\sqrt{2}}, h_3 = \frac{1-\sqrt{3}}{4\sqrt{2}})$  and four wavelet function coefficients  $(g_0 = h_3, g_1 = -h_2, g_2 = h_1, g_3 = -h_0)$  for defining the scale factors  $a$  and the shifting factors  $b$  respectively as shown in the matrix operation below:

$$\begin{bmatrix} \vdots \\ a_i \\ b_i \\ a_{i+1} \\ b_{i+1} \\ a_{i+2} \\ b_{i+2} \\ \vdots \end{bmatrix} = \begin{bmatrix} \ddots & \vdots & \ddots \\ \cdots & h_0 & h_1 & h_2 & h_3 & 0 & 0 & 0 & 0 & \cdots \\ \cdots & g_0 & g_1 & g_2 & g_3 & 0 & 0 & 0 & 0 & \cdots \\ \cdots & 0 & 0 & h_0 & h_1 & h_2 & h_3 & 0 & 0 & \cdots \\ \cdots & 0 & 0 & g_0 & g_1 & g_2 & g_3 & 0 & 0 & \cdots \\ \cdots & 0 & 0 & 0 & 0 & h_0 & h_1 & h_2 & h_3 & \cdots \\ \cdots & 0 & 0 & 0 & 0 & g_0 & g_1 & g_2 & g_3 & \cdots \\ \ddots & \vdots & \ddots \end{bmatrix} \bullet \begin{bmatrix} \vdots \\ S_{2i} \\ S_{2i+1} \\ S_{2i+2} \\ S_{2i+3} \\ S_{2i+4} \\ S_{2i+5} \\ \vdots \end{bmatrix} \quad (11)$$

where  $S_{1-108}$  are the discrete signals.

### 3.3.2 The application of discrete wavelet transformation in time-intensity data processing

In discrete wavelet transform, the signal decomposition process is often be formulated as the combination of two related finite impulse response (FIR) filters, a high-pass filter  $h_{high}$  and a low-pass filter  $h_{low}$  [52]. The FIR filters are used for signal down-sampling ensuring that the transformed signal subspace resolution stays consistent with the original signal. The convolution of  $h_{low}$  and the signal gives the approximation coefficients which are used to reconstruct the denoised signal. The convolution of  $h_{high}$  and the signal outputs the wavelet function coefficients which represent the high-frequency noise.

Workflow of the three-level DWT used in this project is given in Fig.7. The output detail coefficients represent high-frequency noise while the approximation coefficients show low-frequency information. In each DWT step, the input intensity series are down-sampled and the length of the output signal would be  $\frac{N-1}{2}+L$  ( $N$  is the length of the input signal and  $L$  is the length of filters namely 4 in our study). Thus, for each voxel, the length of the time-intensity series would be 19 after the three-level DWT.

The obtained intensity curves after each DWT can be seen in Fig.8 where the first figure is the original TIC and other three are the reconstructed curves using the approximation coefficients. The curves become smooth and noise-free gradually.

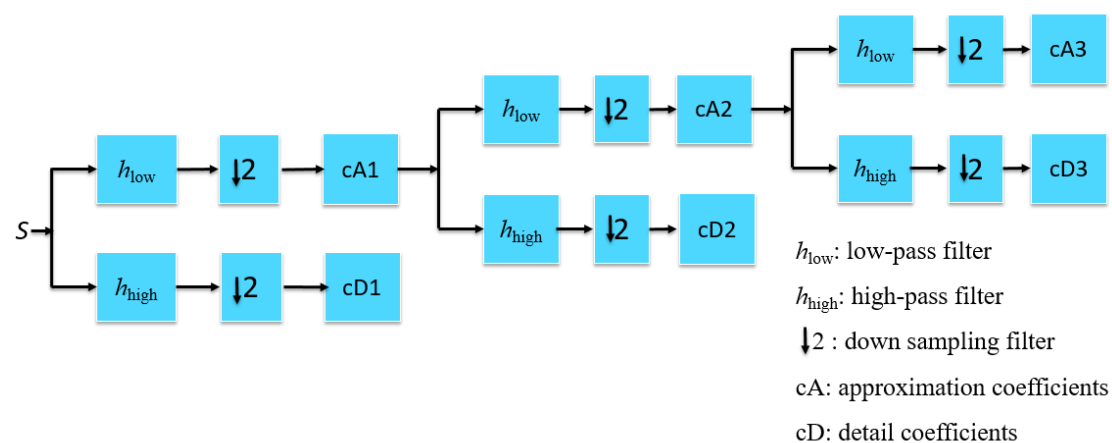


Fig.7. The workflow of level-3 DWT process.

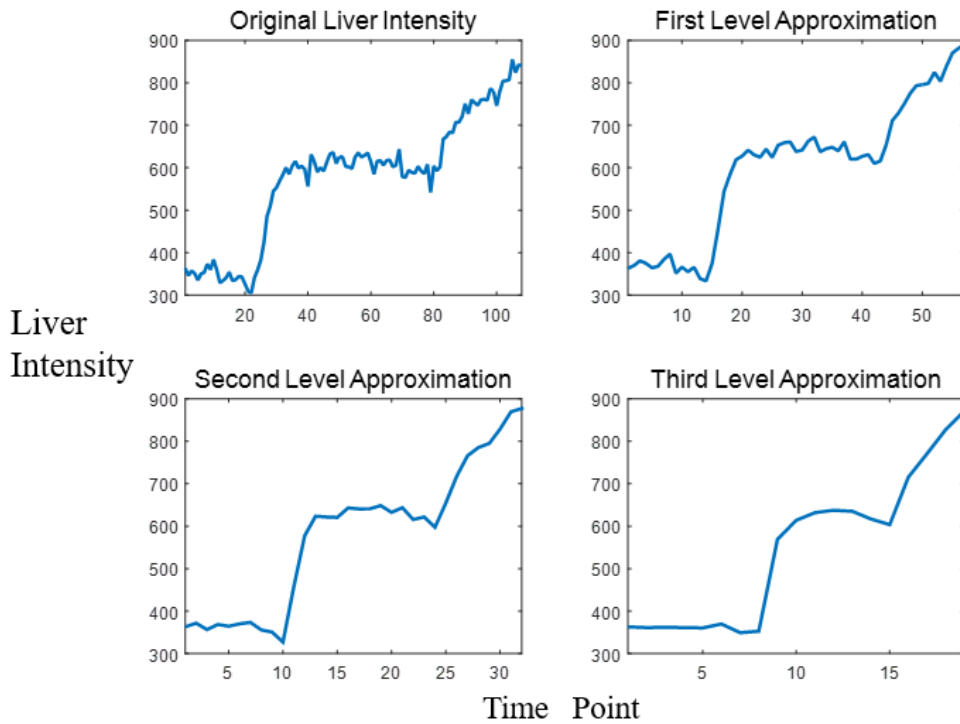


Fig.8. The time-intensity profiles of a pixel in the liver.

## 3.4 DCE-MRI denoising using model fitting

### 3.4.1 Dual-inlet tow compartment liver perfusion model

Model fitting is another effective method for DCE-MRI filtering. Mathematic liver model mimics the CA diffusion process and estimates the CA concentration in hepatocytes. The CA uptake process mainly consists of two stages (see Fig.9). The first stage witnesses CA diffusing from blood vessels (hepatic artery and portal vein) to the extracellular space (the interstitial space between the blood vessel and hepatocytes) driven by the concentration gradient. In the second stage, the specific protein carries CA from extracellular space to hepatocytes causing the second growth in liver TICs. The liver perfusion model proposed by Sourbron [56] was utilized in this study to derive the analytical tissue CA concentration. Based on this concentration, the derivation of signal intensities at each scan time points could be conducted using the transform between them.

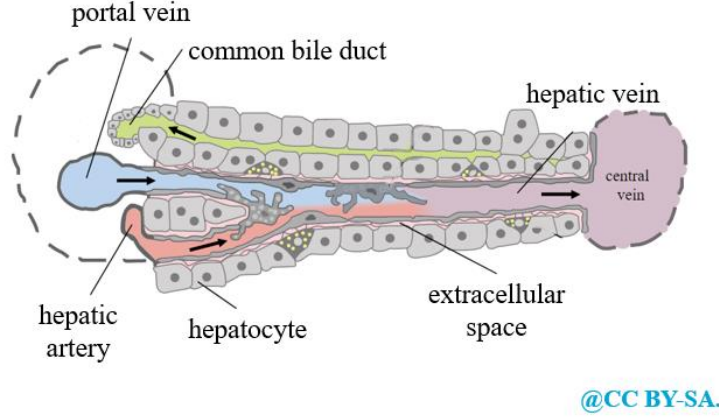


Fig.9. The schematic of the CA uptake process in liver.

As shown in the schematic of liver model Fig.10 [56], the liver is modeled as a sum of two independent spaces namely the interstitial region and hepatocytes. CA inflow starts at both portal vein and hepatic artery. After diffusing into the extracellular space, a part of CA leaves the liver through hepatic veins while the rest is delivered to hepatocytes by the carrier protein. CA excretion relies on the common bile duct. Expressing CA mass conservation in each compartment generates the following equations [56]:

$$V_e \frac{dC_e}{dt}(t) = F_a C_a(t - T_a) + F_v C_v(t - T_a) - (F_a + F_v + K_i) C_e(t) \quad (12)$$

$$V_i \frac{dC_i}{dt}(t) = K_i C_e(t) \quad (13)$$

$$C(t) = [T_e \delta(t) + f_i] * \frac{e^{-\frac{t}{T_e}}}{T_e} * [F_a C_a(t - T_a) + F_v C_v(t - T_a)] \quad (14)$$

where  $V_e$  and  $C_e$  are extracellular volume and concentration respectively,  $V_i$  and  $C_i$  are intracellular volume and concentration,  $F_a$  and  $F_v$  are arterial and venous plasma flows respectively,  $K_i$  is intracellular uptake rate,  $C = C_e V_e + C_i V_i$  is total tissue concentration,  $T_e = V_e / [F_a + F_v + K_i]$  is the extracellular mean transit time,  $f_a = F_a / [F_a + F_v + K_i]$  is the hepatic uptake fraction and  $*$  is the convolution operation. The arterial input function (AIF) and venous input function (VIF) have to be predetermined using the image data. Other five parameters ( $F_a, F_v, T_a, T_v, V_e, K_i$ ) are estimated by means of a nonlinear least squares regression algorithm implemented in Matlab (version R2015a; Mathworks, Natick, USA).

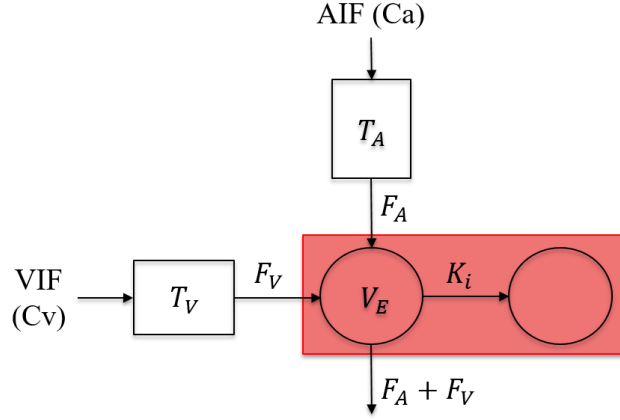


Fig.10. The diagram of Sourbron's liver perfusion model. AIF: arterial input function, VIF: venous input function,  $T_A$  and  $T_V$ : time delay of AIF and VIF,  $F_A$  and  $F_V$ : arterial and venous plasma flow,  $V_E$ : extracellular volume,  $K_i$ : intracellular uptake rate.

### 3.4.2 Measurement of tissue concentration from DCE-MRI

In order to derive the vascular input functions using DCE-MRI data, a transform between signal intensities and tissue CA concentrations is needed. In Sourbron's model, the tissue concentration was calculated as the relative DCE-MR signal enhancement  $S(t)/S_0 - 1$  [56], where  $S(t)$  is the post-contrast signal intensity and  $S_0$  is the pre-contrast signal intensity. However, the signal is not linearly dependent on the CA concentration in MRI. The applied MR scan sequence mainly determines the relationship between the CA concentration and the signal intensities. As it is customary to use gradient echo sequences for DCE-MRI, under steady-state conditions and perfect spoiling of the transverse signal, the following equation holds [55]:

$$S = N(H) \cdot \sin \alpha \cdot \frac{1 - \exp(-TR/T_1)}{1 - \cos \alpha \cdot \exp(-TR/T_1)} \cdot \exp(-TE/T_2^*) \quad (15)$$

in which  $TR$  and  $TE$  are repetition and echo times of the scan sequence respectively,  $\alpha$  is the flip angle,  $N(H)$  is the product of the proton density and an arbitrary factor (the scaling factor used by the scanner) and  $T_1$  is the longitudinal relaxation time.

Due to the assumption that  $TE \ll T_2^*$ , the last exponential term in Eq.(15) can be neglected.  $T_1$  is assumed to be dependent on the longitudinal relaxation time before contrast namely  $T_{10}$ , tissue relaxivity  $\mathbb{R}_1$  and tissue CA concentrations  $C_t$ , shown as

Eq.(16):

$$\frac{1}{T_1} = \frac{1}{T_{10}} + \mathbb{R}_1 C_t \quad (16)$$

Then the concentration can be expressed as follows:

$$\frac{S(t)}{S(0)} = \frac{1 - \exp\left(-TR \cdot \left(\frac{1}{T_{10}} + \mathbb{R}C(t)\right)\right)}{1 - \cos \alpha \cdot \exp\left(-TR \cdot \left(\frac{1}{T_{10}} + \mathbb{R}C(t)\right)\right)} \cdot \frac{1 - \cos \alpha \cdot \exp(-TR/T_{10})}{1 - \exp(-TR/T_{10})} \quad (17)$$

With Eq.(17), MR signal intensities were converted into tissue CA concentrations. The signal intensities at the scan time points also can be derived from the concentrations by the same equation.

### 3.4.3 Global arterial input function (AIF) and venous input function (VIF) measurement

AIF and VIF are expressed as  $C_a$  and  $C_v$  in Eq.(14) respectively indicating CA concentrations in the plasma. In Sourbron's model, these two functions are obtained by averaging the time intensity curves measured voxel-wise in the aorta (cranially from the hepatic artery) and the portal vein. However, this straightforward method cannot give a precise estimation due to the flow of the plasma. Therefore, the obtained numerical results require high computational cost in the convolution operation as well as the parameter estimation. Therefore, the modified AIF model based on Orton's model [57], [58] was used in this project to calculate the analytical solutions of these two vascular input functions.

This model parametrizes the CA flow as a combination of two functions. One describes the CA bolus passage within the plasms expressed as  $C_B(t)$  in Eq.(18). The other shows wash-out of CA in the tail of the vascular input function denoted as  $G(t)$  in Eq.(19).

$$C_B(t) = a_B \mu_B^2 t \exp(-\mu_B t) u(t) \quad (18)$$

$$G(t) = a_G \exp(-\mu_G t) u(t) \quad (19)$$

where  $u(t)$  is the unit step function indicating the transportation delay,  $a_B$

determines the area under the curve of  $C_B(t)$ ,  $a_G$  determines the starting level of the decay function and  $\mu_B$ ,  $\mu_G$  govern the decay rate of the corresponding functions respectively.

In all, the modified AIF model describes the CA diffusion process from blood vessels to extracellular space and decomposes the input function into a bolus shape function and a body transfer function (BTF), shown in Fig.11.

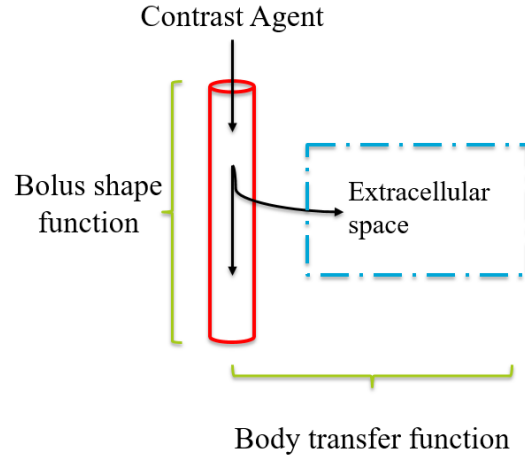


Fig.11. The schematic of AIF model.

The CA concentration in blood plasma is expressed as the superposition of the bolus shape and body transfer functions as following:

$$C(t) = C_B(t - t_0) + C_B(t - t_0) * G(t) \quad (20)$$

where  $t_0$  is the time delay inducing by the bolus transportation.

After substituting  $C_B(t)$  and  $G(t)$  in Eq.(20) with Eq.(18) and Eq.(19), the resulting input function is:

$$C(t) = a_B \mu_B^2 (t - t_0) \left( 1 - \frac{a_G}{\mu_B - \mu_G} \right) \exp^{-\mu_B(t-t_0)} + \frac{a_B a_G \mu_B^2}{(\mu_B - \mu_G)^2} \left( \exp^{-\mu_G(t-t_0)} - \exp^{-\mu_B(t-t_0)} \right) \quad (21)$$

The parameters  $a_B, \mu_B, a_G, \mu_G, t_0$  were estimated by means of a nonlinear least squares regression algorithm implemented in Matlab (version R2015a; Mathworks, Natick, USA).

The fitting goodness of each input function was calculated using Eq.(22) below:

$$\rho=1-\frac{R^2}{\sum(y-\bar{y})^2} \quad (22)$$

where  $R^2$  is the root mean square residual,  $y$  is the measured data and  $\bar{y}$  is the mean of the measured data. The fitting goodness of AIF and VIF are 0.9641 ( $>0.95$ ) and 0.9803 ( $>0.95$ ) showing good matches with the image data. As shown in Fig.12, both AIF and VIF consist of a rapid uptake and a relatively slow decay. The decrease of the decay slope rate is because the active CA transportation is slower than the diffusion process. The enhancement onset time of VIF (about 44s) is around 10 seconds later than AIF's (about 36s) due to the different delivery delays. Meantime, the peak CA concentration in aorta exceeds venous concentration as the portal vein is the downstream side of the aorta.

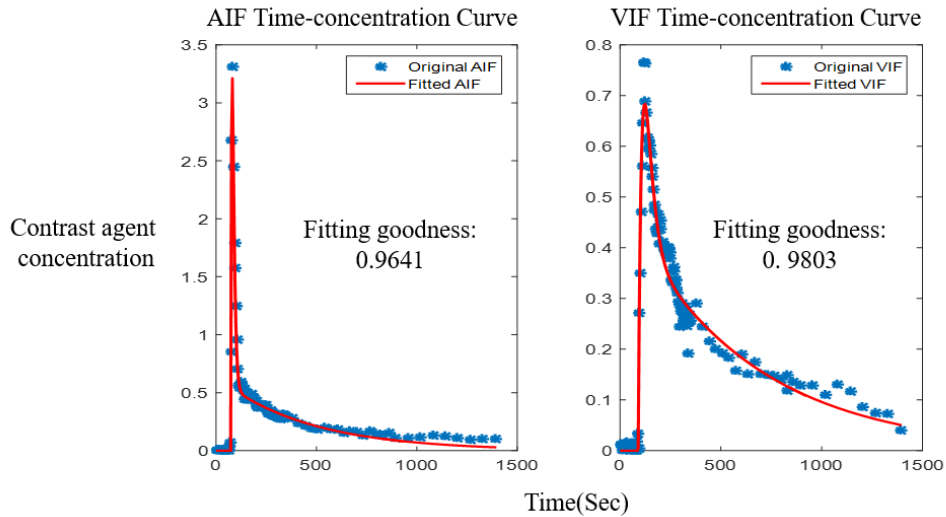


Fig.12. AIF (arterial input function) and VIF (venous input function) obtained from modified Orton's model.

### 3.4.4 TICs obtained from Sourbron's model

After substituting  $C_a$  and  $C_v$  in Eq.(14) with AIF and VIF, the analytical tissue CA concentration can be obtained and thereby the signal intensities at each scan time point using Eq.(17). The obtained TICs are shown in Fig.13. All TICs become smooth significantly and the curve characteristics remain unchanged. Being different from blood vessel's TICs, the liver's keeps increasing over the whole scan period with varying slope rate.

The TICs of relatively large blood vessels such as portal vein and inferior vena cava (IVC) contains a rapid uptake followed by a mild decay. For small vessels like hepatic veins, the signal intensities increase again before the end of image acquisition due to the partial volume effect. At the final stage of the scan, due to the continuous enhancement, the liver intensity exceeds the hepatic vein intensity significantly. Therefore, in those tissues mixed voxels, TICs would rise before scan ending.

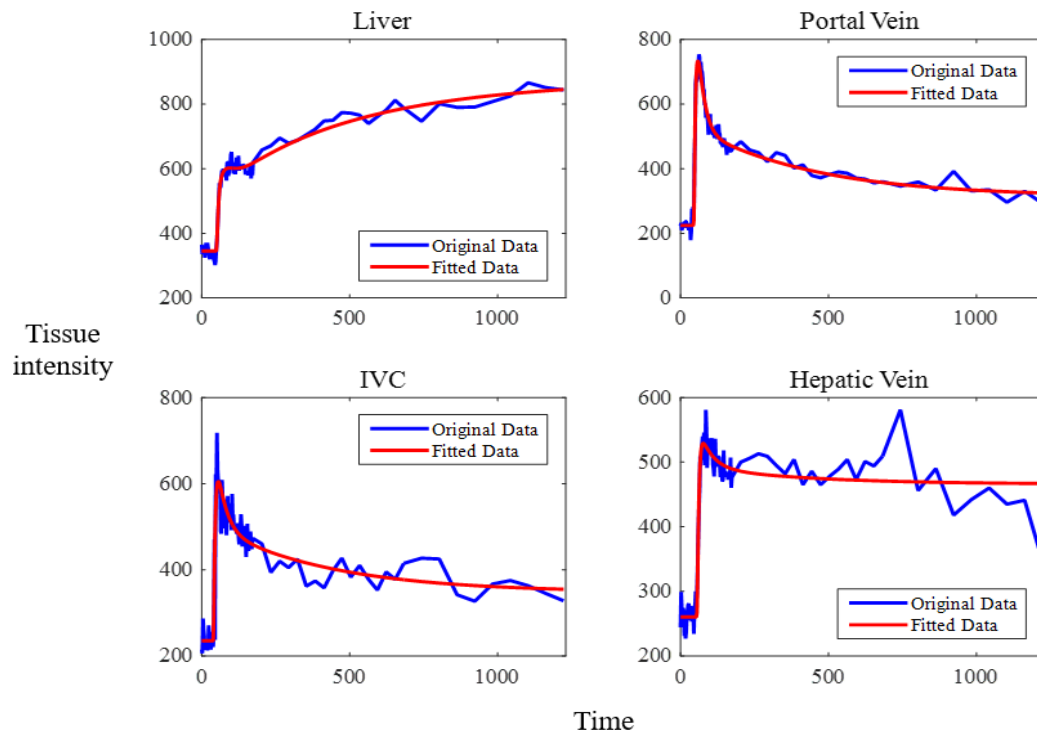


Fig.13. Time-intensity curves obtained from Sourbron’s liver perfusion model.

The red curves are the fitted TICs while the blue curves are the raw TICs. (IVC: inferior vena cava)

### 3.5 Comparison between DWT and model fitting methods

Both DWT and model fitting methods were applied to denoise the DCE-MRI data. DWT method filters the raw data mainly by extracting the low-frequency signal while filtering the high-frequency noise. After applying this method, some intensity information is inevitably sacrificed (the number of image frames is reduced from 108

to 19) due to the down-sampling filters. Because the differences between TICs accumulate over the enhancement period, the reduced image frames make them less significant (see Fig.14). The hepatic vein's TIC peaks at 16<sup>th</sup> time point which is close to the liver's. From the intensity ranks of both hepatic vein and liver TICs, the largest intensity ranks difference is 7 which can be found in the 8<sup>th</sup> and last time points. Nine time points have less or equal to one intensity ranks difference. The small disparity of the intensity ranks could hinder the correlation measurement.

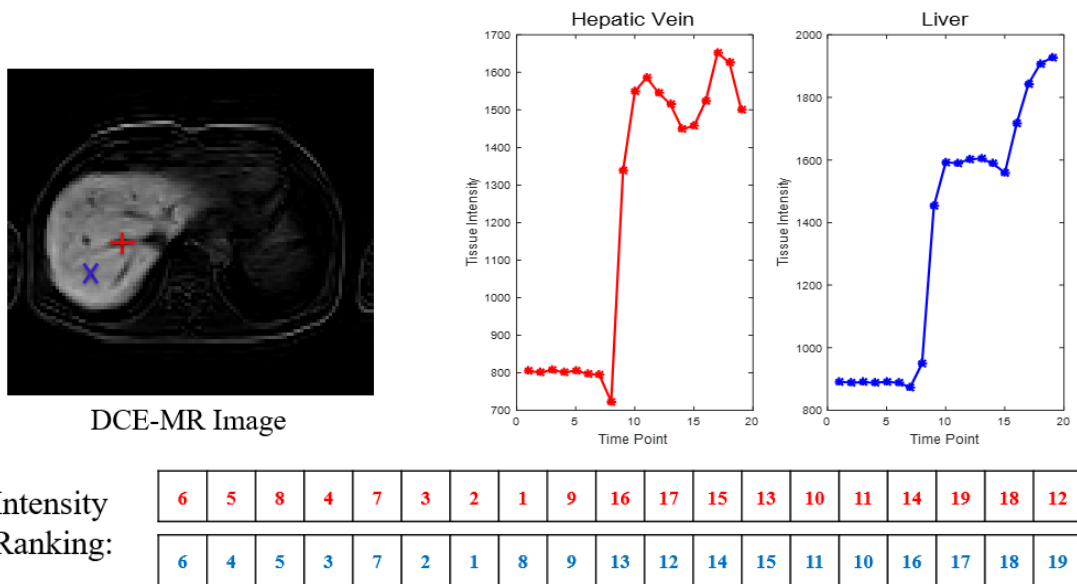


Fig.14. TICs after DWT filtering. The red and blue curves are TICs of a hepatic vein voxel and a liver voxel.

Unlike DWT method, the model fitting method keeps the time series length unchanged. The raw image data were fitted to Sourbron's model to obtain the analytical tissue CA concentration. Then the signal intensities at the corresponding scan time points can be derived based on the CA concentrations, thereby obtaining the denoised TICs. The tissue CA concentration is the convolution product of two input functions (AIF and VIF) and the transfer function between two liver compartments. All these exponential form functions guarantee the continuity of the tissue CA concentration, thereby the smoothness of the derived TICs. TICs acquired from the model fitting were utilized for the vessel segmentation instead of the raw image data. However, the regression analysis in model fitting leads to a high computation cost while in DWT, the computation time for the 4D DCE-MRI is less than 10 minutes.

# Vessel Segmentation Using Time-intensity Information

## 4.1 Overview

In Section 4.2, the weighted Spearman rank correlation is introduced and used to calculate the nonparametric correlation between the selected blood vessel's TICs and the TICs of the other part in the liver for the vessel identification. Subsequently, in Section 4.3, the mixed TIC of each voxel is decomposed by calculating the linear relationship between contributing components. Finally, in section 4.4, the new hybrid level set method introduced in Chapter 2 is applied to the component maps for vessel segmentation.

## 4.2 Spearman rank correlation

Intensity inhomogeneities in MRI as known to lead to intensity variations [42]. As such, tissues cannot be precisely identified using intensity values. In addition, artifacts induced by patient's breathing and motion could further increase signal variation. Accordingly, instead of using parametric correlation methods, the nonparametric Spearman rank correlation which measures TIC shape similarity, was selected in this project.

All the data points in the TIC of each voxel are ranked first. Then the correlation coefficients are calculated with respect to the differences between intensity ranks using Eq.(24) [53]:

$$\rho=1-\frac{\sum_{i=1}^{i=n}(x_i - y_i)^2}{n(n^2 - 1)} \quad (23)$$

where  $x_i$  and  $y_i$  are ranks of the corresponding intensity data and  $n$  is the number of time points which is 108 in our study.

The profile of TICs is expected to represent the intrinsic physical property of different tissues. This rank correlation intends to cluster voxels in terms of the TIC's shape similarity. Three voxels were selected from ROIs inside the portal vein, hepatic veins and liver respectively as the reference TICs. The research region of the correlation calculation was set to be the whole liver mask. To further increase the sensitivity of this correlation method, a weighted Spearman correlation was proposed expressed as Eq.(25):

$$\rho=1-\frac{\left( w_1 \sum_{i=1}^{i=n_1} (x_i - y_i)^2 + w_2 \sum_{i=n_1+1}^{i=n_2} (x_i - y_i)^2 + w_3 \sum_{i=n_2+1}^{i=108} (x_i - y_i)^2 \right)}{n(n^2 - 1)} \quad (24)$$

where  $n_{1-2}$  are predetermined to divide the whole enhancement period into three subsets ( $n_1 = 40, n_2 = 81$ ).

The curve slope rate changes between each subset (see Fig.15). In the first two subsets, the two CA diffusion stages (blood vessels uptake and diffusion from the blood plasms to the extracellular space) dominate.

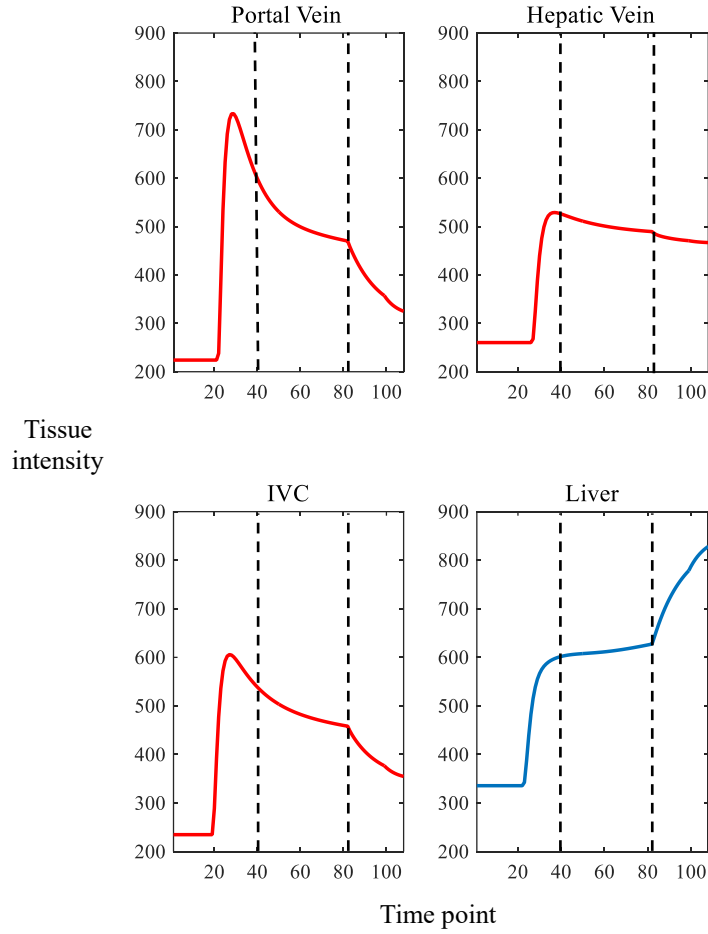


Fig.15. The division of the whole enhancement period. (IVC: inferior vena cava)

For blood vessels, the weights  $w_{1-3}$  were set to be 1.7, 1.5 and 1 respectively, while for liver, they were set to be 1, 1 and 2. The first and second subsets of vessel TICs were given higher weights because the intensity variations within these two subsets can differentiate vessel voxels from the liver. Meanwhile, the liver TIC peaks at the end of the last subset, therefore higher weight was given to the last one. Fig.16 shows the obtained correlation maps. The high contrast between vessels and the liver can be seen in them. In the portal vein correlation map (a), the portal vein region has the highest correlation coefficients (around 1) while the lowest coefficients are in the liver region ( $< -0.5$ ). In the hepatic vein correlation map (b), the contrast between hepatic veins (around 0.5) and liver ( $\leq 0$ ) is less obvious due to the partial volume effect. Meanwhile, in liver correlation maps (c) and (d), the liver region has higher values than the vessel regions.

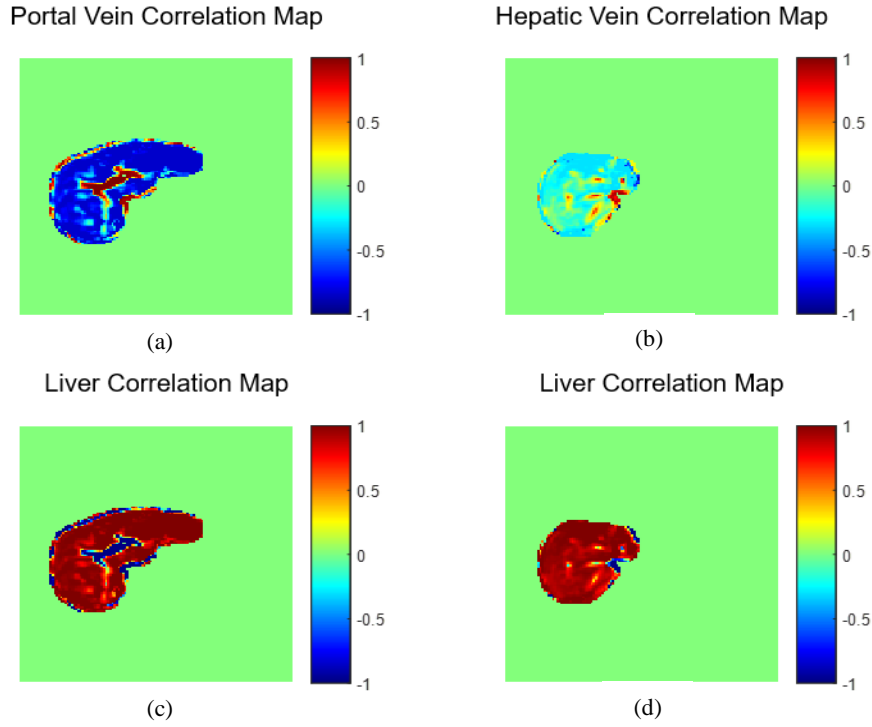


Fig.16. The correlation coefficient maps with portal vein, hepatic vein and liver TICs as the references.

### 4.3 Mixing estimation map

The high contrast between the interior vessel and liver regions was obtained using the weighted Spearman rank correlation. To further define the vessel boundaries, the mixing estimation method proposed by Gutierrez DR [59] was applied. This method is based on the assumption that the TIC of a certain voxel ( $I_{total}$ ) is the linear combination of all contributing TICs. In our study, we assumed that TICs of the voxels at edges of vessels are a linear combination of both the vessel's TIC ( $I_1$ ) and the liver's TIC ( $I_2$ ), as illustrated in Fig.17. The pure vessel TICs were selected from ROIs in the vessel center.

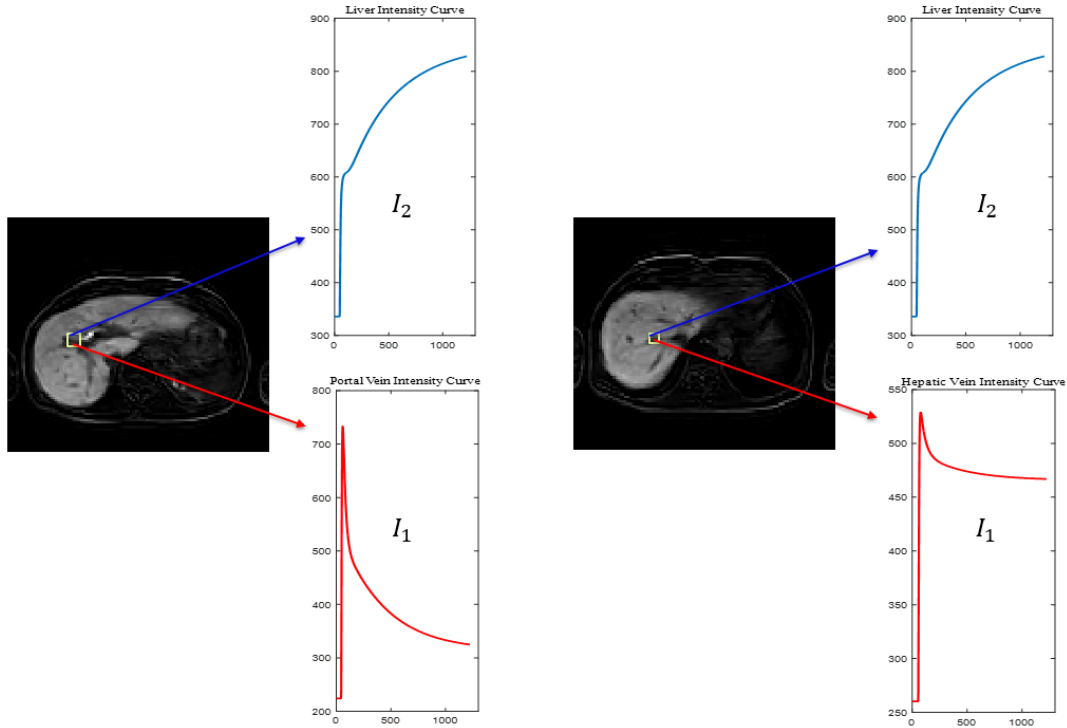


Fig.17. The schematic of the linear mix assumption. The y axes are the tissue intensity while the x axes are the time.

The mixed TIC in a voxel is expressed as  $I_{total} = \alpha_1 I_1 + \alpha_2 I_2 + \alpha_3 I_3 + \alpha_4 I_4$  where  $\alpha_{1-3}$  are fractions of portal vein, hepatic vein and IVC respectively,  $\alpha_4$  is liver's fraction,  $I_{1-3}$  are TICs of the vessels and  $I_4$  is liver tissue's TIC. In mixing estimation maps shown in Fig.18, the vessel regions have higher values than liver regions and a gradient can be found from the vessel center to the boundary. The higher value of a certain voxel in vessel's estimation maps indicates that the vessel's TIC takes a larger fraction than the liver tissue's TIC in the linear combination. With these mixing estimation maps, the contrast between the vessel exterior boundaries and the liver could be attained.

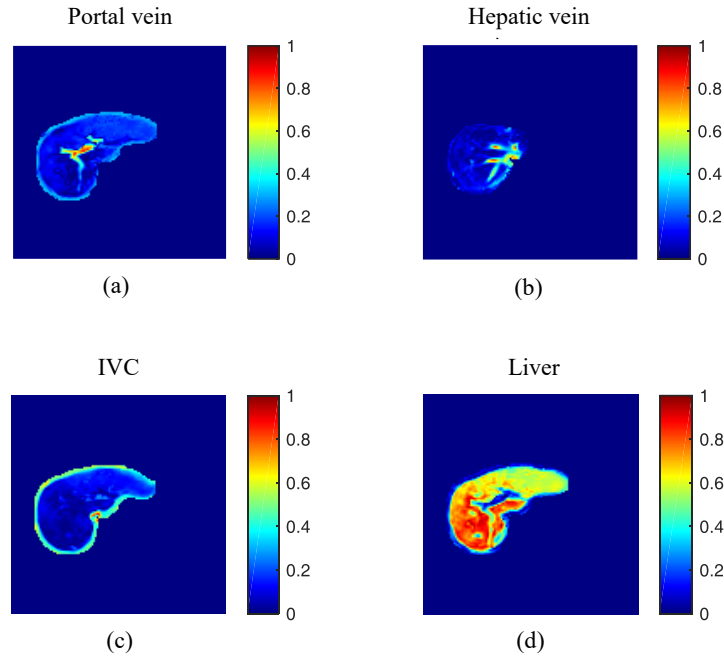


Fig.18. The mixing estimation maps. Maps (a), (b) and (c) represent the fraction of the corresponding vessel's TICs in the linear combination. Map (d) is the fraction of liver tissue's TIC. In IVC (inferior vena cava) fraction map (c), the boundary has high fractions. The liver mask was dilated twice to ensure that all vessel voxels are included. Therefore, those boundary voxels are not from liver leading to high values in IVC map.

## 4.4 Vessel segmentation using new hybrid level set method

The new hybrid level set method introduced in Chapter 2 enables a robust and accurate segmentation [45]. The summation of the correlation maps and the mixing estimation maps was used as the input of the new hybrid level set method to improve the segmentation in boundary voxels, which is illustrated in Fig.19. In the summation maps, all vessel regions have positive values while the liver regions stay negative. Therefore, the threshold for level set segmentation could be easily selected. The maximum image gradient only exists between the vessel and the liver giving a specific indication about object's boundary location for the level set contour.

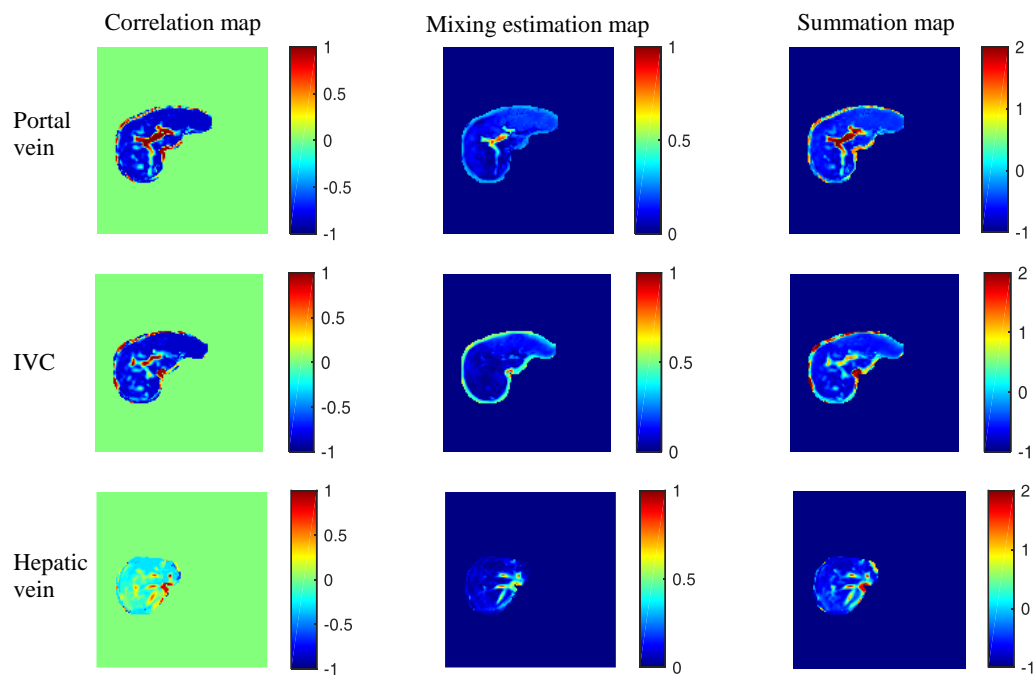


Fig.19. The figures of mixing estimation maps, correlation maps and summation maps of the selected slices. (IVC: inferior vena cava)

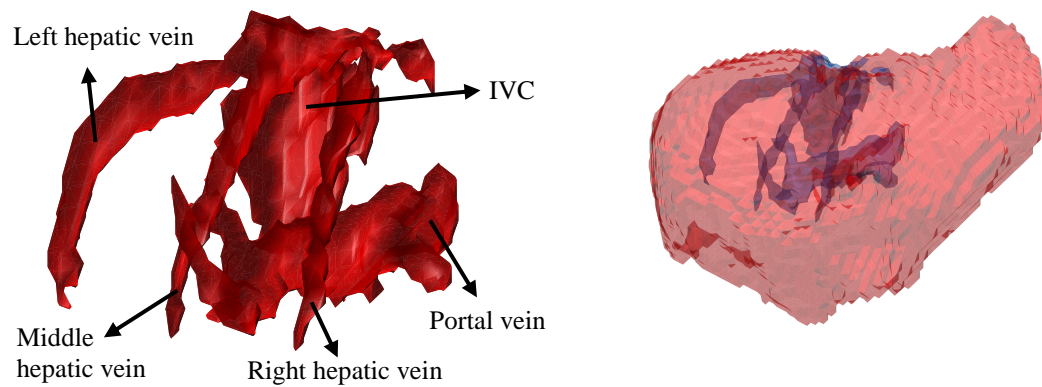


Fig.20. The obtained 3D vessel structure. (IVC: inferior vena cava)

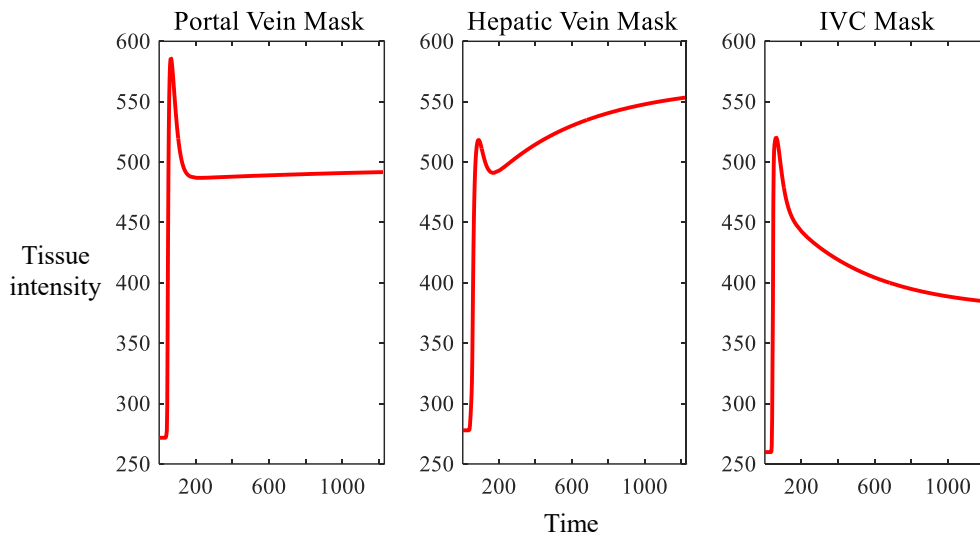


Fig.21. The mean TIC of each vessel mask. (IVC: inferior vena cava)

The segmentation result is presented in Fig.20. The main branches of the portal vein, hepatic veins and IVC were segmented. The mean TIC of the three vessel masks were calculated individually shown in Fig.21. The mean TIC of IVC is consistent with the vessel diffusion characteristic that a quick uptake is followed by a relatively slow decay. In both portal vein and hepatic vein mask, the partial volume effect alters the intensity variation direction in the final enhancement period. But still, a significant decay which enables the differentiation between vessels and liver can be found in the curve after the first enhancement. The obtained vessel masks were applied to the functional liver segmentation in the below chapter.

## 4.5 Vessel segmentation method verification and comparison

The DCE-MR images of eleven patients were obtained in our study. The proposed vessel segmentation method has been applied to seven clinical cases while the other three cases were excluded in this study because the tumors occupy more than half of the liver in those patients. Among all these seven cases, excluding one normal case (case 1), the other six all have visible lesions inside the liver.

In order to verify the proposed method, an evaluation was performed by

calculating the average symmetric surface distance (ASSD) and modified Hausdorff distance (MHD) between the manual and proposed segmentations [5], [64], [65]. The manual segmentation was conducted using the last frame of the DCE-MRI in MITK (2016.11). The vessel boundaries were excluded in the manual segmentation due to the insufficient contrast in the image however included in the proposed segmentation owing to the mixing estimation map (see Fig.22). Accordingly, the exterior boundary voxels in the proposed segmentation would be regarded as the background voxels in the manual segmentation yielding a low specificity.

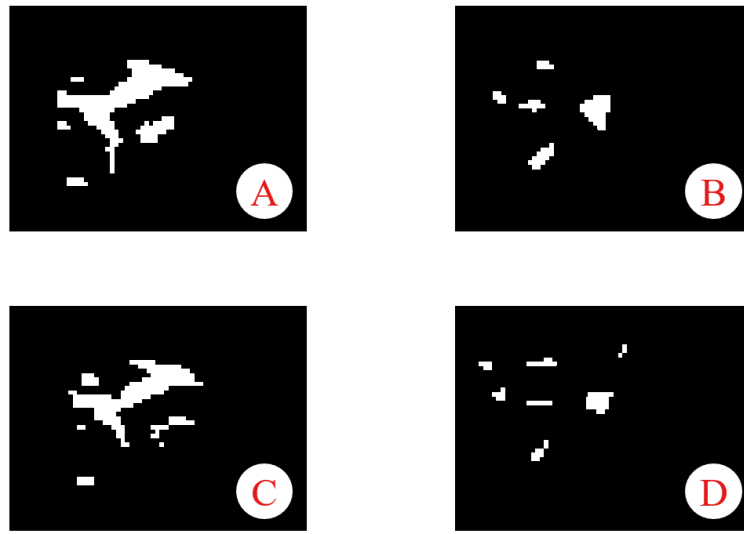


Fig.22. The comparison between the manual and proposed segmentations. Figures A and B are results of the proposed segmentation while figures C and D are results of the manual segmentation.

The ASSD and MHD were calculated according to the following equations [5], [64]:

$$ASSD = \frac{\sum_{a \in A} \min_{b \in M} \|a - b\| + \sum_{b \in M} \min_{a \in A} \|a - b\|}{2(N_A + N_M)} \quad (25)$$

$$MHD(A, B) = \max \left\{ \frac{1}{N_A} \sum_{a \in A} \min_{b \in M} \|a - b\|, \frac{1}{N_M} \sum_{b \in M} \min_{a \in A} \|a - b\| \right\} \quad (26)$$

where A and M denote the surfaces of the automatically and manually segmented objects, a and b are points on A and B respectively.  $\|a - b\|$  is the distance between a and b.  $N_A$  and  $N_M$  are the numbers of points on A and M.

Tab.1 gives ASSD and MHD of both proposed approach and diffusion enhancing filter (DEF) based segmentation method adopted in Luu's study [8]. The obvious ASSD variations between cases can be found in the DEF method. In the cases which have relatively large tumors such as case 2, the ASSD and MHD of the DEF approach increase significantly. The anisotropic diffusion inside the tumor increases the uncertainty of the DEF method, as this method is based on the assumption that the anisotropic diffusion only takes place in vessels [7], [60]. As both the tumor and vessels are enhanced after the filtering, the region growing method fails to separate them.

The MHD values of the proposed method are in the range of about 3.0 *mm* to 5.2 *mm* while for DEF method, the values vary from around 5.0 *mm* to 27.8 *mm*. From ASSD, values for the proposed method are all below 4.8 *mm* whereas values for DEF method have a significant variation with an overall mean 7.3776 *mm*. The smaller ASSD and MHD in the proposed method indicate the smaller level of error. The segmentations of the proposed method are more stable regardless of whether the patient has a tumor or not.

|                     | Level set             |                      | DEF                   |                      |
|---------------------|-----------------------|----------------------|-----------------------|----------------------|
|                     | ASSD<br>( <i>mm</i> ) | MHD<br>( <i>mm</i> ) | ASSD<br>( <i>mm</i> ) | MHD<br>( <i>mm</i> ) |
| <b>Case 1</b>       | 3.2685                | 3.4071               | 3.8721                | 5.0523               |
| <b>Case 2</b>       | 2.7444                | 3.0189               | 16.5477               | 27.7962              |
| <b>Case 3</b>       | 3.2448                | 3.4392               | 5.5107                | 8.9901               |
| <b>Case 4</b>       | 2.7198                | 2.7798               | 6.5010                | 8.4453               |
| <b>Case 5</b>       | 3.0579                | 3.1491               | 7.0278                | 8.9145               |
| <b>Case 6</b>       | 3.1968                | 3.2565               | 4.8333                | 7.8696               |
| <b>Case 7</b>       | 4.7625                | 5.2431               | 7.3512                | 11.4810              |
| <b>Overall mean</b> | <b>3.2850</b>         | <b>3.4704</b>        | <b>7.3776</b>         | <b>11.2212</b>       |

Tab.1. Comparison of ASSD and MHD for all seven clinical cases segmented with the proposed level set method and diffusion enhancement filtering method.

# Functional Liver Partition

## 5.1 Overview

In Section 5.2, the resection planes are defined and interpolated to the liver mask for partition. Subsequently, in Section 5.3, the functional liver partition method is applied to five clinical cases and the volume of each segment is calculated.

## 5.2 Resection plane interpolation

The functional liver partitioning is carried out according to Couinaud's classification using the resection planes [62], [63]. For the vertical partition, three resection planes crossing the three hepatic veins were defined respectively using the matrix operation below:

$$\begin{pmatrix} x_1 & y_1 \\ x_2 & y_2 \end{pmatrix} \begin{pmatrix} A \\ B \end{pmatrix} = \begin{pmatrix} 1 \\ 1 \end{pmatrix} \quad (27)$$

Before constructing the resection planes, the coordinates of the three landmarks on the hepatic veins and one on the IVC were picked from the vessel mask projection image (see Fig.23). The three vertical planes were constructed using each two of these four points respectively. Referring to Fig.27, the left plane divides 7, 6 and 8, 5 segments. The middle plane separates 8, 5 and 4a, 4b segments. 2, 3 and 4a, 4b segments are divided by the right plane.

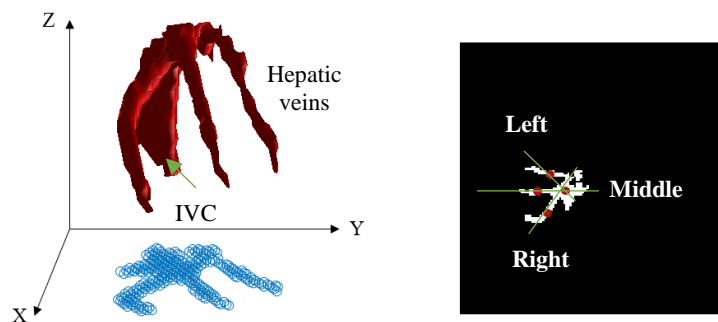


Fig.23. Determination of three landmarks on hepatic veins and one on IVC. The left figure shows the X-Y plane projection of the vessel mask. The red points in the right figure indicate the selected landmarks for resection planes construction.

In Couinaud's classification, the first segment is defined as the region between the portal vein bifurcation and IVC. According to this, two vertical planes from the portal vein bifurcation to the IVC's right and left edges were interpolated and, accompanying by IVC, a closed and triangle alike area was constructed to approximate the first segment (see Fig.24). Points 1 and 2 on the IVC edge were selected based on the maximal distance between them. The line from point 3 to IVC center is perpendicular to the line between 1 and 2 points and thereby it was selected.

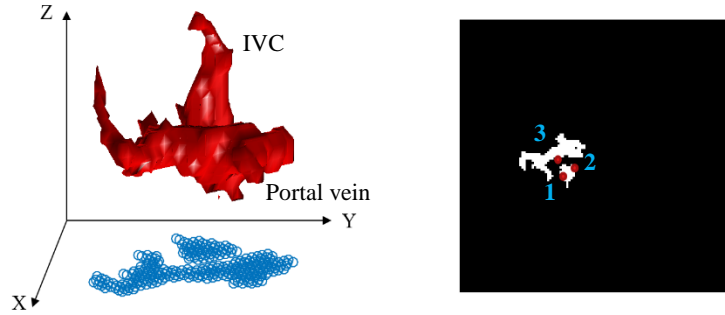


Fig.24. Determination of three landmarks for the first segment. The left figure shows the X-Y plane projection of the vessel mask. The red points in the right figure indicate the selected landmarks for resection plane construction. Point 3 on the portal vein bifurcation edge while the other two 1 and 2 points on the IVC edge were selected.

The portal vein bifurcates into right and left branches when it goes into the liver. After this main bifurcation, the two separated branches continue to part into two sub-branches respectively. The horizontal planes interpolated for superior and inferior liver lobes partition were determined by these secondary bifurcations. The projection in X-Z plane of portal vein mask (see Fig.25) was used for resection plane positioning. The slices where the left and right secondary bifurcations located at were selected to segment the left and right liver lobes.

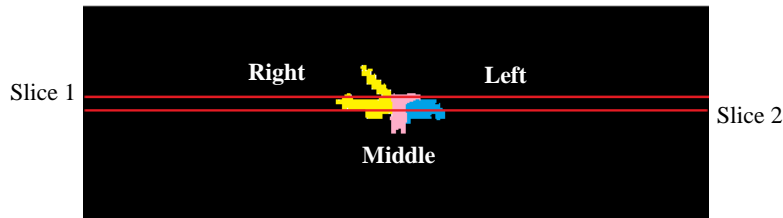


Fig.25. Determination of horizontal resection planes. The projection image consists of the right, middle and left portal vein, the corresponding yellow, pink and blue regions. The two red lines slice 1 and slice 2 indicate the slice locations of the right and left portal vein bifurcations respectively.

## 5.3 Functional liver partition

With the well-defined resection planes in Section 5.2, the eight independent segments could be determined using the plane equation  $Ax + By = 1$ . The detailed workflow for the partition process is shown in Fig.26. Tab.2 lists the conditions to define the eight liver segments. Each segment consists of voxel points  $(x, y, z)$  which meet the corresponding conditions. The first segment was calculated and excluded before other segments were determined. This proposed functional partition method has been applied to the cases (case 1, 4, 5, 6, and 7) which have the full vessel structure (three hepatic veins, the portal vein and IVC) in the previous vessel segmentation. The different views of the partition result are shown in Fig.27 and each segment is marked by one specific color.

The volume of each segment is calculated using the voxels number multiplied by the voxel size ( $3 \times 3 \times 5 \text{mm}^3$ ) as presented in Tab.3. Since the lesions have already been excluded during the liver segmentation, the volume of those unhealthy cases could be smaller. For instance, in case 5, a tumor located at the third segment yields a significantly smaller volume.

In all, the volume of each segment varies between patients. The comparison between manual and proposed partitions is in demand for verification.

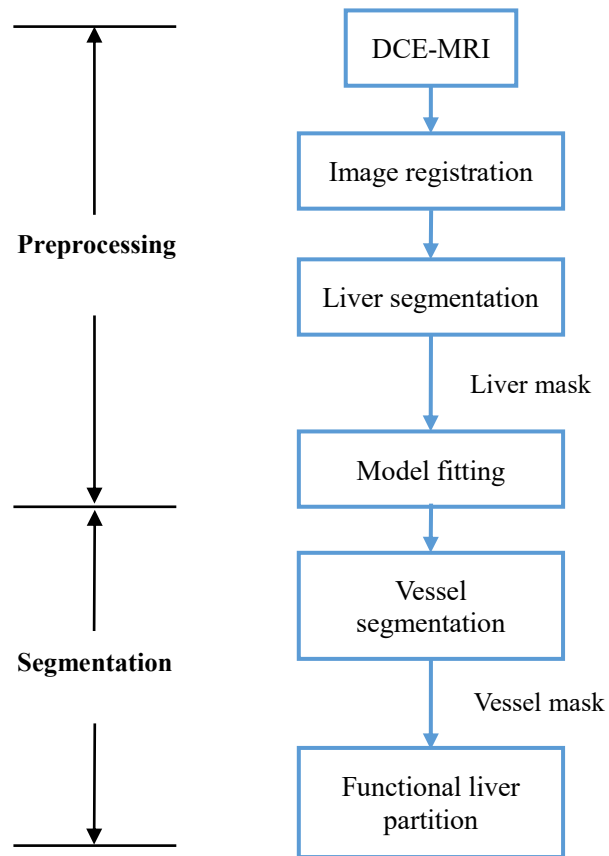


Fig.26. Workflow of the proposed functional liver partition.

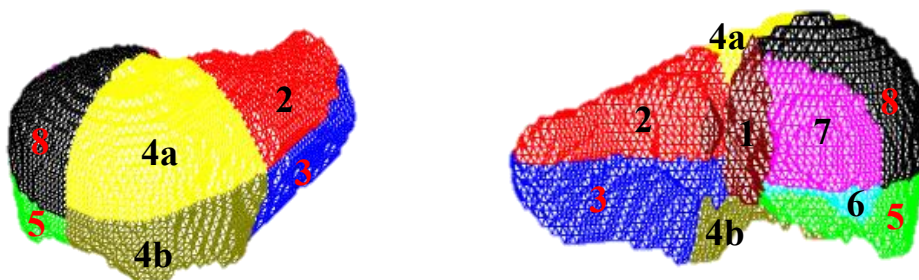


Fig.27. Liver functional segments.

| Segment     | Defining conditions   |
|-------------|---|
| <b>I</b>    | $xA_L + yB_L > 1, xA_R + yB_R > 1$                              |
| <b>II</b>   | $xA_{LHV} + yB_{LHV} > 1, z > z_{PVB}$                          |
| <b>III</b>  | $xA_{LHV} + yB_{LHV} > 1, z < z_{PVB}$                          |
| <b>IVa</b>  | $xA_{LHV} + yB_{LHV} < 1, xA_{MHV} + yB_{MHV} < 1, z > z_{PVB}$ |
| <b>IVb</b>  | $xA_{LHV} + yB_{LHV} < 1, xA_{MHV} + yB_{MHV} < 1, z < z_{PVB}$ |
| <b>V</b>    | $xA_{RHV} + yB_{RHV} < 1, xA_{MHV} + yB_{MHV} > 1, z < z_{PVB}$ |
| <b>VI</b>   | $xA_{RHV} + yB_{RHV} > 1, z < z_{PVB}$                          |
| <b>VII</b>  | $xA_{RHV} + yB_{RHV} > 1, z > z_{PVB}$                          |
| <b>VIII</b> | $xA_{RHV} + yB_{RHV} < 1, xA_{MHV} + yB_{MHV} > 1, z > z_{PVB}$ |

Tab.2. Conditions defining each liver segment. *A* and *B* are the constant parameters for each plane definition. (*L*: left, *R*: right, *LHV*: left hepatic vein, *MHV*: middle hepatic vein, *RHV*: right hepatic vein, *PVB*: portal vein bifurcation)

| Segment      | <b>I</b><br>( <i>cm</i> <sup>3</sup> ) | <b>II</b><br>( <i>cm</i> <sup>3</sup> ) | <b>III</b><br>( <i>cm</i> <sup>3</sup> ) | <b>IVa</b><br>( <i>cm</i> <sup>3</sup> ) | <b>IVb</b><br>( <i>cm</i> <sup>3</sup> ) | <b>V</b><br>( <i>cm</i> <sup>3</sup> ) | <b>VI</b><br>( <i>cm</i> <sup>3</sup> ) | <b>VII</b><br>( <i>cm</i> <sup>3</sup> ) | <b>VIII</b><br>( <i>cm</i> <sup>3</sup> ) |
|--------------|--|---|--|--|--|--|---|--|---|
| <b>Case1</b> | 18.31                                  | 231.21                                  | 269.23                                   | 142.87                                   | 109.75                                   | 155.79                                 | 23.35                                   | 42.52                                    | 192.96                                    |
| <b>Case4</b> | 24.34                                  | 283.72                                  | 76.86                                    | 267.48                                   | 144.36                                   | 333.54                                 | 29.20                                   | 274.68                                   | 424.84                                    |
| <b>Case5</b> | 20.83                                  | 181.75                                  | 1.57                                     | 182.70                                   | 49.90                                    | 299.02                                 | 181.93                                  | 225.18                                   | 320.35                                    |
| <b>Case6</b> | 30.87                                  | 135.63                                  | 102.37                                   | 115.69                                   | 222.16                                   | 465.93                                 | 170.37                                  | 247.00                                   | 268.06                                    |
| <b>Case7</b> | 6.12                                   | 340.96                                  | 171.04                                   | 234.13                                   | 242.82                                   | 277.51                                 | 117.94                                  | 256.18                                   | 157.81                                    |

Tab.3. The volume of each segment.

## Discussion and Conclusion

### 6.1 Overview

In Section 6.2, the limitations of the proposed vessel segmentation method are discussed. Subsequently, in Section 6.3, the limitations of the proposed functional liver partition method are given. In Section 6.4, the possible improvements for both vessel segmentation and functional liver partition are illustrated. Finally, in Section 6.5, the conclusions of this thesis project are interpreted.

## 6.2 Limitations of hepatic vessel segmentation

The vessel segmentation approach proposed in this thesis fulfills the automatic segmentation based on 4D DCE-MRI. The voxels clustering procedure was conducted by the correlation measurement with the reference TICs. The rapid uptake followed by a slow decay intensity variation in vessel TICs dominates the differentiation. Therefore, the artifacts such as the partial volume effect and the patient's breathing and motion which might alter the TIC shape, could affect the accuracy of this method. Although the weighted Spearman correlation was applied to enhance the sensitivity of this approach, some vessel boundary voxels still have negative correlation. For example, as shown in Fig.28, the red circled region in the left DCE-MR image could easily be identified as portal vein region according to the lower intensity, however in the right correlation map, it has a negative correlation with the reference portal vein TIC.

Additionally, referring to Tab.1, the segmentation in case 7 gives higher ASSD and MHD than other cases. Part of portal vein as well as hepatic veins are enclosed by the tumor in this case. Those inside tumor vessel voxels have negative correlation due to the partial volume effect. Meanwhile, the tumor TIC is not included in the mixing estimation map calculation. As a result, those voxels are ruled out in the segmentation leading to the inaccurate result.

Besides, the correlation map accuracy was largely depended on the input TICs, thereby requiring user supervision.

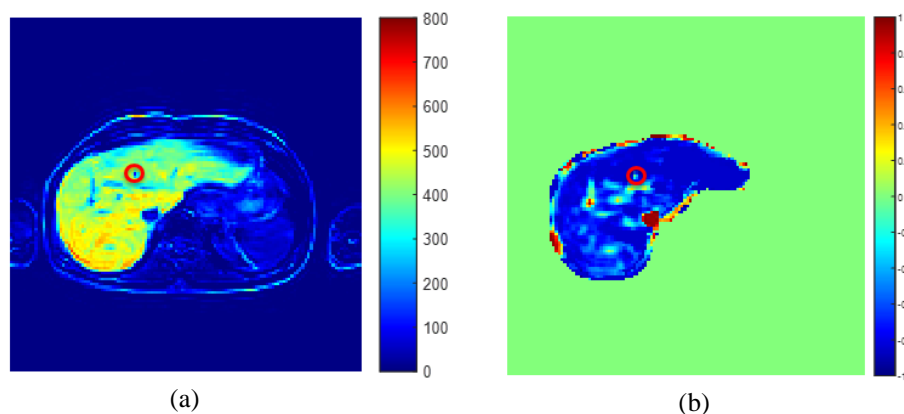


Fig.28. Image (a) is the minus product of the last DCE image frame and the first DCE image frame. Image (b) is the portal vein correlation map.

In despite of all the limitations mentioned above, the continuousness of the vessel junctions was preserved with this proposed segmentation and thus, the computation for connected component analysis could be saved. In addition, the threshold-based segmentation was replaced by the level set method. The mixing estimation map allows the vessel exterior boundaries to be included in the segmentation.

### 6.3 Limitations of functional liver segmentation

The resection planes for functional liver partition were defined as the vertical and horizontal planes crossing the corresponding vessels. In Couinaud's classification, however, both the planes and the locations of the gallbladder and falciform ligament are used in the partition [17]. For the left lobe partition, radiologists use the location of falciform ligament to define the resection plane rather than the left hepatic vein [17]. In most cases, the left hepatic vein is not a straight line and it heads for the left liver from the middle. But in this project, the left resection plane was constructed by considering the straight part of the left hepatic vein, and thus yields inaccuracies. Besides, the right hepatic vein might bifurcate after the IVC trifurcation (see Fig.29). The vertical resection plane should be interpolated along the blue dashed line.

In addition, the first segment should be a region enclosed by the portal vein bifurcation boundary and IVC theoretically [17]. In this project, the triangle region was used to approximate it, which may lead to a smaller segment volume.

Meanwhile, manual inputs for vessel landmarks determination were required. Although the distance clustering algorithm has been approved to meet the automaticity requirement, it demands the vessel sub-branches to be included in the segmentation [61]. Due to the limited image resolution in this study, full segmentation of the vessel sub-branches can be a challenge. Hence, the automatic functional partition method requires further researches.

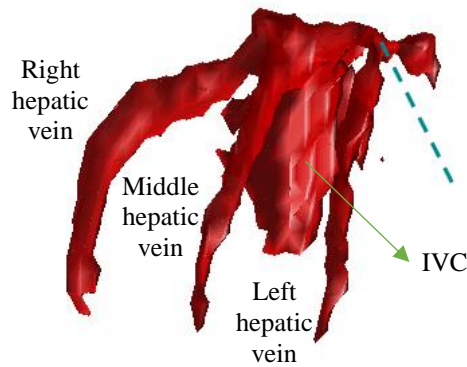


Fig.29. Bifurcation of left hepatic vein. (IVC: inferior vena cava)

## 6.4 Future Improvements

This TIC shape based vessel segmentation method requires that the TICs are consistent with the tissue intrinsic properties. Therefore, the artifacts such as the patients' breathing and partial volume effect which might change the TIC shape, should be compensated during the image preprocessing stage.

The vessel segmentation method has been applied to seven cases and the complete segmentation has only been achieved in five of them due to the tumors. For those patients who have relatively large tumors in their livers, the tumor could enclose or distort the vessels leading to incomplete segmentation. Therefore, the segmentation of the tumor enfolded vessels calls for further research.

For the functional liver partition, the curve fitting method for resection plane construction might be able to delineate each segment more precisely due to the curved vessel shapes but also may consume greater computation. The first segment definition could be improved by using the portal vein bifurcation boundary curve rather than planes.

The same principle developed in this thesis project could be extended to the organ segmentation. The liver correlation map could be used to verify the liver segmentation result.

## 6.5 Conclusions

The vessel segmentation and functional liver partition methods developed in this thesis intend to provide better visualization for 4D DCE-MRI. In image preprocessing stage, all DCE-MRI data were fitted to Sourbron's model for noise filtering. The analytical solutions of both AIF and VIF were obtained using the modified AIF model in order to have more accurate estimations for the vascular input functions. Then the signal intensities at the corresponding scan time points could be derived from the analytical tissue CA concentrations.

The weighted Spearman correlation algorithm measured the similarity between tissue TICs. The added weights intended to improve the sensitivity of the algorithm in capturing the intensity variations. The mixing estimation approach conducted the parametric analysis of DCE-MRI data to further define those low correlation voxels. The sufficient contrast between the vessel and liver regions in the summation maps gave a specific indication about the object boundary location. The new hybrid level set method was used for auto-segmentation and only 2 to 3 iterations were required for the precise segmentation owing to the high image contrast. Both interior and exterior vessel boundaries were included in the segmentation.

All resection planes were defined through the simple matrix operation. The landmarks for plane interpolation were selected from the vessel mask projection images. Therefore, the determination of the liver segments was largely depended on how accurate the vessels were segmented in the previous step.

In all, this thesis project proposed a time-intensity information based vessel segmentation method and a functional liver partition method for the DCE-MRI. The partition provides a better visualization for the liver surgery planning and the treatment follow-up.

# References

- [1] Yankeelov TE, Gore JC, “Dynamic Contrast Enhanced Magnetic Resonance Imaging in Oncology: Theory, Data Acquisition, Analysis, and Examples. Current medical imaging reviews,” 3(2):91-107 (2009).
- [2] Dário AB Oliveira, “Segmentation of liver, its vessels and lesions from CT images for surgical planning,” BioMedical Engineering OnLine (2011).
- [3] Luc Soler, “Fully automatic anatomical, pathological and functional segmentation from CT scans for hepatic surgery,” Comput Aided Surg (2001).
- [4] Aradhana M Venkatesan, “Liver Segmental Anatomy and Analysis from Vessel and Tumor Segmentation via Optimized Graph Cuts,” Springer-Verlag Berlin Heidelberg (2012).
- [5] Marija Marcan, “Segmentation of hepatic vessels from MRI images for planning of electroporation-based treatments in the liver,” Radiol Oncol (2014).
- [6] Alejandro F. Frangi, “Multiscale Vessel Enhancement Filtering,” Springer Verlag, Berlin, Germany, pp. 130-137 (1998).
- [7] Rashindra Manniesing, “Vessel enhancing diffusion a scale space representation of vessel structures,” Elsevier B.V. (2006).
- [8] H. M. Luu, “Quantitative evaluation of noise reduction and vesselness filters of liver vessel segmentation on abdominal CTA images,” Phys Med Biol, vol. 60 (2015).
- [9] Mahapatra D, “Joint Segmentation and Groupwise Registration of Cardiac Perfusion Images Using Temporal Information,” Journal of Digital Imaging. 26(2):173-182 (2013).
- [10] Francesco Conversano, “Hepatic Vessel Segmentation for 3D Planning of Liver Surgery: Experimental Evaluation of a New Fully Automatic Algorithm,” Academic radiology (2011).
- [11] R.J. Maciunas, “Interactive Image-Guided Neurosurger,” Park Ridge, IL; American Association of Neurological Surgeons, pp. 17-44 (1993).
- [12] F. G. Zöllner, “Assessment of 3D DCE-MRI of the kidneys using nonrigid image

- registration and segmentation of voxel time courses,” *Comput. Med. Imaging Graph.*, vol. 33, no. 3, pp. 171–181 (2009).
- [13] D. Zikic, “Automatic alignment of renal DCE-MRI image series for improvement of quantitative tracer kinetic studies,” *Proc. SPIE*, vol. 6914, pp. 691432-691432–8 (2008).
- [14] M. P. Heinrich, “MIND: Modality independent neighbourhood descriptor for multimodal deformable registration,” *Med. Image Anal.*, vol. 16, no. 7, pp. 1423–1435 (2012).
- [15] Oliver Gloger, “Fully Automated Renal Tissue Volumetry in MR Volume Data Using Prior-Shape-Based Segmentation in Subject-Specific Probability Maps,” *Biomedical Engineering IEEE Transactions on*, vol. 62, pp. 2338-2351 (2015).
- [16] R. Adams and L. Bischof. “Seeded region growing,” *IEEE Trans. on Pattern Analysis and Machine Intelligence*, 16(6):641–647 (1994).
- [17] Robin Smithuis and Eduard E. de Lange, “Anatomy of the liver segments,” Radiology Department of the Alrijne Hospital, Leiderdorp, the Netherlands and University of Virginia Health System, Charlottesville, USA (2012).
- [18] Saulius Rutkauskas, Vytautas Gedrimas, “Clinical and anatomical basis for the classification of the structural parts of liver,” *Medicina (Kaunas)* 42(2) (2006).
- [19] Derek L G Hill, Philipp G Batchelor and Mark Holden, “Medical image registration,” *Phys. Med. Biol.* 46 R 1-R45 (2001).
- [20] L. G. Brown. “A survey of image registration techniques,” *ACM Computing Surveys*, 24(4):325—376 (1992).
- [21] WoodsRP, “Automated image registration: I. general methods and intrasubject, intramodality validation,” *J Comput Assist Tomo.* 22(1):139–152 (1998).
- [22] AshburnerJ, FristonKJ, “Nonlinear spatial normalization using basis functions,” *Hum Brain Mapp*, 7:254–266 (1999).
- [23] HermosilloG, Chef'd'HotelC, FaugerasO, “Variational methods for multimodal image matching,” *Int J Comput Vis.* 50(3):329–343 (2002).
- [24] OrchardJ, “Globally optimal multimodal rigid registration: an analytic solution using edge information,” In: *Proceedings of the IEEE International Conference on Image Processing*, San Antonio, TX, USA. p. 485–488 (2007).
- [25] PluimJPW, MaintzJBA, ViergeverMA, “Mutual information based registration of medical images: a survey,” *IEEE Trans Med Imaging.* 22(8):986–1004 (2003).

- [26] Maes F, Vandermeulen D, Suetens P, “Medical image registration using mutual information,” *Proc IEEE*. 91(10):1699–1722 (2003).
- [27] Gefen S, Tretiak O, Nissanov J, “Elastic 3-D alignment of rat brain histological images,” *IEEE Transactions on Medical Imaging* 22(11):1480-1489 (2003).
- [28] Shen D, Davatzikos C, “HAMMER: hierarchical attribute matching mechanism for elastic registration,” *IEEE Transactions on Medical Imaging* 21(11):1421-1439 (2002).
- [29] M. C. Morrone, R. A. Owens, “Feature detection from local energy,” *Pattern Recognition Letters*, 6, 303-313 (1987).
- [30] Mattias P. Heinricha, Mark Jenkinson and Manav Bhushan, “MIND: Modality independent neighbourhood descriptor for multi-modal deformable registration,” *Medical Image Analysis*, Vol 16 (2012).
- [31] M. Hassaballah, H.A. Alshazly, “Image Features Detection, Description and Matching,” Springer International Publishing Switzerland (2016).
- [32] Antoni Buades, “Self-similarity based Image Denoising,” *Communications of the ACM*, Vol.54 No.5 (2011).
- [33] F. Maes, “Multimodality image registration by maximization of mutual information,” *IEEE Transactions on Medical Imaging*, pp. 187-198 (1997).
- [34] C. Wachinger, N. Navab, “Entropy and laplacian images: structural representations for multi-modal registration,” *Medical Image Analysis*, pp. 1-17 (2012).
- [35] Dinesh D. Patil and Sonal G. Deore, “Medical Image Segmentation: A Review,” *IJCSMS*, Vol.2, Issue.1, pg.22-27 (2013).
- [36] Heimann, T., I. Wolf, and H.P. Meinzer, “Active shape models for a fully automated 3D segmentation of the liver - An evaluation on clinical data,” *Medical Image Computing and Computer-Assisted Intervention - Miccai* (2006).
- [37] Zhang, X., “Automatic liver segmentation from CT scans based on a statistical shape model,” *Conference proceedings : Annual International Conference of the IEEE Engineering in Medicine and Biology Society. IEEE Engineering in Medicine and Biology Society. Conference* (2010).
- [38] Kass, M., A. Witkin, and D. Terzopoulos, “Snakes: Active contour models,” *International Journal of Computer Vision* (1988).
- [39] Chen, Y.F., “Liver Segmentation from CT Images Based on Region Growing

- Method,” 3rd International Conference on Bioinformatics and Biomedical Engineering, Vols 1-11 (2009).
- [40] Li, M. and Z. Lei, “Liver Contour Extraction using Snake and Initial Boundary Auto-Generation. in Bioinformatics and Biomedical Engineering,” The 2nd International Conference (2008).
- [41] Sethian, J., “Level Set Methods and Fast Marching Methods: Evolving Interfaces,” Computational Geometry (1998).
- [42] Chunming Li, “A Level Set Method for Image Segmentation in the Presence of Intensity Inhomogeneities With Application to MRI,” IEEE Transactions on image processing, VOL 20 (2011).
- [43] M. Kass, A. Witkin, and D. Terzopoulos, “Snakes: Active contour models,” Journal of Computer Vision, 1:321-331 (1987).
- [44] Gavriil Tschepnakis, “Deformable Model-Based Medical Image Segmentation,” Medical Image Segmentation and Registration Methodologies: Volume 1 (2011).
- [45] Yan Zhang, Bogdan J. Matuszewski, Lik-Kwan Shark, “Medical Image Segmentation Using New Hybrid Level-Set Method,” IEEE (2008).
- [46] C. Li, “A variational level set approach to segmentation and bias correction of medical images with intensity inhomogeneity,” in Proc. Med. Image Comput. Aided Intervention (2008).
- [47] C. Samson, “A variational model for image classification and restoration,” IEEE Trans. Pattern Anal. Mach. Intell., vol. 22 (2000).
- [48] Tian Zhang, “Improved registration of DCE-MR images of the liver using a prior segmentation of the region of interest,” SPIE (2016).
- [49] Indulekha N R, M Sasikumar, “Medical image denoising using three dimensional discrete wavelet transform and bilateral filter,” International Journal of Management and Applied Science, ISSN:2394-7926 (2015).
- [50] Daniel T.L. Lee, Akio Yamamoto, “Wavelet Analysis: Theory and Applications,” Hewlett-Packard Journal (1994).
- [51] Sheng Li, Frank G. Zollner and Andreas D. Merrema, “Wavelet-based segmentation of renal compartments in DCE-MRI of human kidney: Initial results in patients and healthy volunteers,” Computerized Medical Imaging and Graphics 36 108– 118 (2012).
- [52] R. Gonzalez and R. Woods, “Digital Image Processing,” Prentice Hall,

Englewood Cliffs, NJ (2002).

- [53](n.d.). Retrieved July 01, 2017, from <https://readtiger.com/wkp/en/Liver>.
- [54]O. Kubassova, R. D. Boyle, A. Radjenovic, “Quantitative analysis of dynamic contrastenhanced MRI datasets of the metacarpophalangeal joints,” *Academic Radiology*, 14(8): 1189–1200 (2007).
- [55]Lavini C, de Jonge MC, van de Sande MGH, “Pixel-by-Pixel analysis of DCE-MRI curve patterns and an illustration of its application to the imaging of the musculoskeletal system,” *Magnetic Resonance Imaging* 25:604-612 (2007).
- [56]Steven Sourbron, “Combined Quantification of Liver Perfusion and Function with Dynamic Gadoteric Acid-enhanced MR Imaging,” *Radiology: Volume 263* (2012).
- [57]Matthew R Orton, James A d’Arcy and Simon Walker-Samuel, “Computationally efficient vascular input function models for quantitative kinetic modelling using DCE-MRI,” *Institute of Physics and Engineering in Medicine* (2008).
- [58]JN van Schie, “Estimating the AIF from DCE-MRI Data with Compensation for Flow Enhancement (I): Theory, Method and Phantom Experiments,” *Journal of Magnetic Resonance Imaging* (2016).
- [59]Gutierrez DR, “Partial volume effects in dynamic contrast magnetic resonance renal studies,” *Eur J Radiol* (2010).
- [60]Bachir Taouli, “Diffusion-weighted MR Imaging of the Liver,” *Radiology*, Volume 254, Issue 1 (2010).
- [61]Yufei Chen, “Functional Region Annotation of Liver CT Image Based on Vascular Tree,” *BioMed Research International* (2016).
- [62]Ola Kristoffer Oye, “Illustrative Couinaud Segmentation for Ultrasound Liver Examinations,” *Springer-Verlag Berlin Heideberg* (2011).
- [63]YAN Fat-Kin, “Automatic Segmentation of Functional Hepatic Segments on Computed Tomography,” *The HKU Scholars Hub* (2011).
- [64]Marie Pierre Dubuisson, “A Modified Hausdorff Distance for Object Matching,” *Proc. International Conference on Pattern Recognition, Jerusalem, Israel* (1994).
- [65]Wang G, “A new segmentation framework based on sparse shape composition in liver surgery planning system,” *Med Phys* (2013).